Department of Construction Sciences
Solid Mechanics

ISRN LUTFD2/TFHF-20/5237-SE(1-46)

Correlation of numerical simulation methods and failure criteria to experimental burst test

Master's Dissertation by

Karlo Kasljevic

Supervisors:
Assoc. Prof. Ralf Denzer, Div. of Solid Mechanics
M.Sc. in Physical Engineering Per Ekedahl, GKN Aerospace

Examiner:
Assoc. Prof. Håkan Hallberg, Div. of Solid Mechanics

Printed by Media-Tryck AB, Lund, Sweden
For information, address:
Division of Solid Mechanics, Lund University, Box 118, SE-221 00 Lund, Sweden
Webpage: www.solid.lth.se

Abstract

Predicting the burst speed of turbine rotors is a costly and challenging task. Therefore, the scope of this thesis is to perform a correlation study between numerical simulation methods and failure criteria to experimental over-speed burst test of the Prometheus turbine rotor. The rotor was manufactured using selective laser melting, and *GKN Aerospace* performed the over speed burst test, which is the foundation of the project. *ANSYS Mechanical 19.1* was used to perform structural linear elastic and elasto-plastic analysis. Two Hockett Sherby hardening models and linear interpolation of raw hardening data were applied to compute the elasto-plastic analysis. The simulation results were used to calculate several burst margins yielding promising results, with the lowest error margin being approximately 1%. Furthermore, elasto-plastic results proved to be the most accurate for estimating the burst speed, with an error margin of approximately 0.2%. Finally, predicting the location where the fracture is most likely to occur was done by applying the Rice & Tracey criteria, which gave promising results.

Preface

This research is a result of my passion for computational mechanics to develop accurate and precise methods so that simulations correlate better with experiments. More so, being able to perform my research towards the space industry.

I would like to thank and show my gratitude towards my supervisors, colleagues, and the ROTORS department at *GKN Aerospace Sweden*. Without the collaboration of these parties, my research would not be possible. And my most genuine gratitude towards Per Ekedahl for his valuable inputs and guidance. Lastly, I genuinely want to thank my family and friends, who have always helped and supported me.

Karlo Kasljevic,
Trollhättan, June 2020.

Contents

1 Introduction

1.1 Background

GKN Aerospace Sweden develops and manufactures several components and modules for the European Ariane launcher vehicles. The components experience tremendous structural loads were failure could lead to catastrophic downfall. Therefore the components undergo several costly tests ensuring their reliability.

Ariane 6 is currently under development and will be the newest addition to the Ariane-family as of 2020-2021. It is a medium- to heavy-lift launch vehicle able to carry a payload of up to 11500 kg to geostationary transfer orbit. In 2025 the next-generation Ariane 6 launcher vehicles will use the new Prometheus rocket engine. The Prometheus rocket turbine will drive two turbo-pumps, these turbine modules are developed and manufactured by GKN Aerospace Sweden.

Redesigning the turbine is required to reach the new specifications to cope with several liftoffs and higher loads for the next-generation Ariane Launcher vehicles. The Prometheus single-stage turbine is currently under development and will be the scope of the project.

1.1.1 Prometheus rocket turbine

The single-stage Prometheus rocket turbine seen in Fig. 1.1 will be replacing the previous Vulcan 2.1 two-stage rocket turbine used in Ariane 5 and will be used in the next-generation Ariane 6 engine. It drives two turbopumps, pumping methane and oxygen to the rocket engine. It is manufactured using additive manufacturing, specifically selective laser melting.

1.2 Problem description and project goals

During liftoff, the turbine components experience tremendous structural loads were failure could lead to catastrophic downfall. Therefore the components undergo several costly tests ensuring their reliability. To reduce development costs, various softwares are used to estimate the limitations of these components. The accuracy of these simulations is crucial and requires validation by correlating the results to real-life experimental testing. Overspeed burst experiment was conducted on the Prometheus demonstrator turbine rotor, enabling a correlation study to be conducted between experimental tests and simulation results, validating the accuracy of over-speed failure simulations.

The objective of the thesis is to re-examine the results of the performed experimental burst test and the beforehand over-speed simulation study of the Prometheus demonstrator turbine rotor, increasing the understanding of over-speed burst. Furthermore, elastic and elasto-plastic simulations are to be conducted using *ANSYS Mechanical*

Figure 1.1: Prometheus demonstrator rotor.

19.1 to obtain accurate over-speed burst estimations and results. Finally, several burst criteria shall be applied and compared to validate their accuracy.

1.3 Limitations

The material model will be based upon elastic and multi kinematic hardening relations, from data obtain purely from 3D printed mechanical tensile test experiments, which are assumed to be isotropic. Furthermore, the static structural simulations will not take temperature and time into consideration. Only quasi-static simulations will be conducted to reduce computational time.

2 Theory

2.1 Material behavior

General established theories of material behavior which applies to metals in general will be discussed in this chapter. The relationship between stress and strain, describing the deformation which is obtained for a given load is called a constitutive relation.

2.1.1 Linear elasticity

When material is lightly loaded it will exhibit a linear relation between stress and strain, this region is called the elastic region and when unloaded will return to its original configuration. This linear stress-strain relationship which characterizes most solid materials was suggested by Hooke in 1676 and is called Hooke's law, defined as

$$\sigma_{ij} = D_{ijkl}\epsilon_{kl} \tag{1}$$

where σ_{ij} is the stress tensor, ϵ_{ij} is the strain tensor and D_{ijkl} denotes the elastic stiffness tensor.

Properties of most metals are not direction dependent, they exhibit isotropic properties. This reduces the number of independent parameters in the elastic stiffness tensor down to two, denoted as Lames parameters, μ and λ. Rewriting the linear elastic stress-strain relation from Hooke's law Eq. (1), generates

$$\sigma_{ij} = \lambda\epsilon_{kk}\delta_{ij} + 2\mu\epsilon_{ij} \tag{2}$$

where,

$$\lambda = \frac{\nu E}{(1+\nu)(1-2\nu)}, \qquad \mu = \frac{E}{2(1+\nu)} \tag{3}$$

here ν denotes Poisson's ratio, E is the Young modulus and δ is the Kronecker delta. The isotropic elastic stiffness tensor D_{ijkl}, can now be derived from Eqs. (2) & (3):

$$D_{ijkl} = 2\mu\left[\frac{1}{2}(\delta_{ik}\delta_{jl} + \delta_{il}\delta_{jk} + \frac{\nu}{1-2\nu}\delta_{ij}\delta_{kl})\right] \tag{4}$$

The stress tensor σ_{ij}, can be split into two terms, the deviatoric stress tensor S_{ij}, and the hydrostatic stress tensor σ_{Hyd} [1, 2], defined as:

$$\sigma_{ij} = S_{ij} + \sigma_{Hyd}\delta_{ij}, \qquad \sigma_{Hyd} = \frac{1}{3}\sigma_{kk} \tag{5}$$

2.1.2 Kinematic and Isotropic hardening rules

Loading material past its elastic phase reaching its yield point, it will start to permanently deform, see Fig. 2.1 point A. After the yield point, the material enters its hardening phase, also know as work-hardening or strain-hardening, which permanently changes the yield point and can be described by hardening rules. The material

still contains its elastic energy after entering the plastic phase. Thus when unloaded, it will retain a new configuration C and not B. This phenomenon is called elastic recovery.

Isotropic hardening rule is characterized by an equally increasing tensile yield point as a compressive yield point. Indicating that the yield surface remains in the same position and holds its shape but expands equally in all directions. Kinematic hardening rule instead moves the position of the yield surface, containing its shape and size. This reduces the compressive yield point if the tensile hardening occurs. This phenomenon is called the Bauschinger effect, see Fig. 2.2.

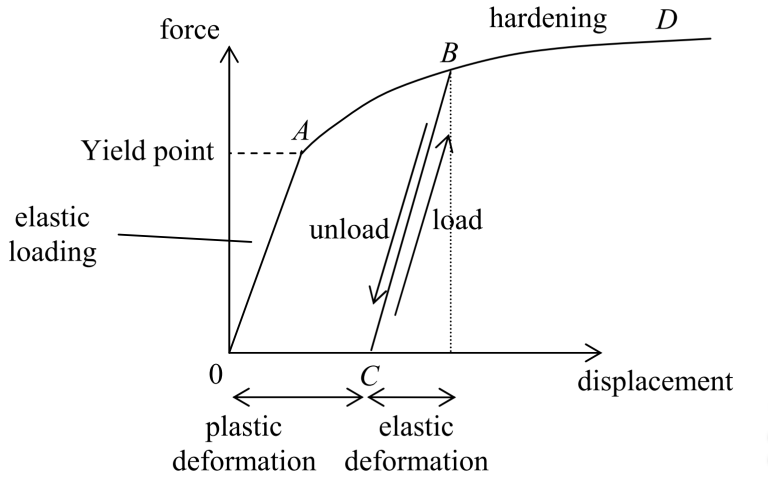

Figure 2.1: Force-displacement curve for an elastic material[2].

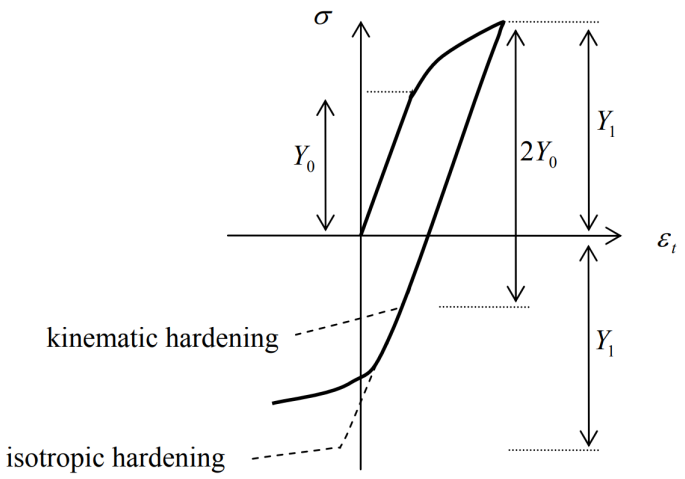

Figure 2.2: Visualization of isotropic and kinematic hardening along with the Bauschinger effect[2].

2.2 Experimental tensile tests

Performing tensile tests is common in engineering practices to determine valuable information and properties of the material. This information can be used in structural analysis, modeling, design, and further developing new material. Recorded data is used to plot stress-strain curves and obtain information about properties such as ultimate tensile strength, yield strength, Young's modulus, hardening, and softening phase.

2.2.1 Engineering stress and strain

Engineering stress is obtained by dividing the applied force F with the smallest cross-section area A_0 of the specimen. Likewise, the engineering strain is calculated by dividing the elongation δ by the original gauge length, L_0.

$$\sigma = \frac{F}{A_0}, \qquad \epsilon = \frac{\delta}{L_0} \tag{6}$$

2.2.2 True Stress and strain

True stress and true strain takes into account the shrinking of the cross-section area and the developed elongation further elongating, respectively. True stress and strain are defined by the following equations[3].

$$\sigma_t = \frac{F}{A} = \sigma(1+\epsilon) \qquad \epsilon_t = \int \frac{\delta L}{L} = ln(1+\epsilon) \tag{7}$$

Calculating the slope of the linear part at the beginning of the stress-strain curve yields the elastic modulus. Furthermore, by observing where the engineering stress-strain curve crosses the standard 0.2% offset of Young's modulus slope, one can pinpoint the yield point. Taking the cross-section shrinking and the elongation development into account, the stress-strain curve starts to diverge due to the stress increase, see Fig. 2.3.

2.3 Material hardening models

Material hardening models are used to describe the non-linear behavior that occurs after the linear elastic phase. Several constitutive models have been developed for this reason, trying to describing the hardening behavior of different types of material.

2.3.1 Bilinear and multilinear isotropic hardening model

The bilinear isotropic hardening model is commonly used to describe the hardening phenomenon of metals. The model characterizes the hardening phase as linear strain-hardening after reaching the yield point, where the slope of the curve in the plastic region is called tangent modulus.

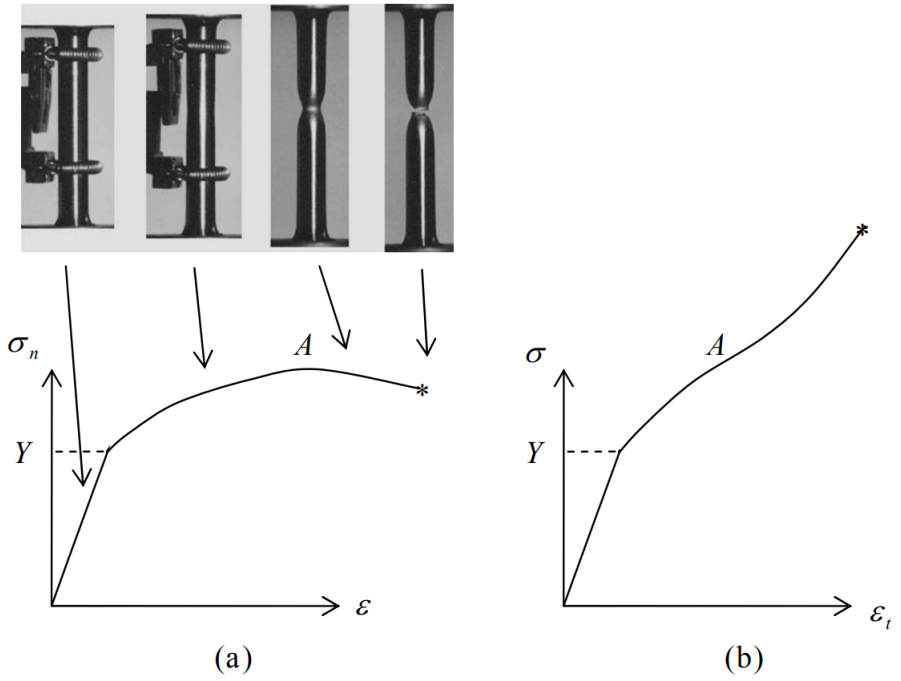

Figure 2.3: Stress-strain curves. (a) Engineering stress-strain curve, (b) true stress-strain curve[2].

The multilinear isotropic hardening model is an extension of the bilinear model; it applies several linear tangents to describe the hardening phenomenon in the plastic region.

2.3.2 Hockett Sherby hardening law

Applying tensile test data can be problematic due to noise in the raw data and large oscillation after yield in the stress-strain curve, the later is more present in tensile tests performed at high temperatures. Material hardening models and curve fitting methods are therefore used to generate stress-strain curves suitable for usage.

The Hockett-Sherby hardening law utilizes exponential polynomial function to curve fit the true stress-strain curve. The stress-strain relation was proposed by Hockett and Sherby in 1975 while curve-fitting large strain compression data of polycrystalline and iron material at room temperature[4].

$$\sigma_{t,HS} = A - exp(-(k\epsilon_t)^n)(\sigma_s - \sigma_y) \tag{8}$$

Where $\sigma_{t,HS}$ represents the true stress calculated using Hockett Sherby hardening law, A denotes the steady-state flow stress, σ_y is the yield stress, ϵ_t denotes the true strain and n along with k are constants, where the latter is associated with the strain-hardening characteristics of the material. Further simplifying the relation Eq. (8),

one can group the constants.

$$\sigma_{t,HS} = A - exp(-k^n \epsilon_t^n)B \tag{9}$$

$$\sigma_{in,HS} = A - B \cdot exp(-m\epsilon_{in}^n) \tag{10}$$

Finally, modeling only the hardening phase was done by denoting the true stress and strain to inelastic stress and strain, where inelastic strain ϵ_{in} is defined as

$$\epsilon_t = \epsilon_{el} + \epsilon_{in} = \frac{\sigma_t}{E} + \epsilon_{in} \quad \Rightarrow \quad \epsilon_{in} = \epsilon_t - \frac{\sigma_t}{E} \tag{11}$$

2.4 Fracture criteria

Fracture criteria are developed to try and model when and where failure will occur to better predict and improve the safety margins on the construction. In this thesis this subject is limited to over-speed burst criteria on disc and rotor type constructions where the temperature is not accounted for.

2.4.1 Area weighted mean hoop stress criteria

Hoop stress also called cylinder or circumferential stress is defined as normal stress in the tangential direction. The *area weighted mean hoop stress* criteria also called Robinsons criteria is defined as[5]

$$BM_{Hoop} = \sqrt{\frac{\sigma_{UTS}}{\bar{\sigma}_\theta}} \tag{12}$$

In words, burst will occur when mean hoop stress equals and surpasses the ultimate tensile strength of the material. σ_{UTS} denotes the ultimate engineering tensile strength of the material and $\bar{\sigma}_\theta$ the mean hoop stress. For a volumetric finite element implementation of the criteria the mean hoop stress or mean tangential stress is calculated as

$$\bar{\sigma}_\theta = \frac{\sum_{elem=e}^{n}(V^e \cdot \sigma_\theta^e)}{\sum_{elem=e}^{n}(V^e)} \tag{13}$$

where n denotes the total number of elements, V^e the element volume and σ_θ^e the element tangential stress.

The National Aeronautics and Space Administration (NASA) further developed the area weighted mean hoop stress criterion by performing several experimental burst tests, thus established the burst factor F_b trough empirical data[6].

$$BM_{Hoop,\,NASA} = \sqrt{\frac{F_b \cdot \sigma_{UTS}}{\bar{\sigma}_\theta}} \tag{14}$$

The burst factor F_b, also called material utilization factor (MUF) is dependent on the ductility of the material and the design factor F_d of the disc, see Fig. 2.4. F_d

is a measurement of how nearly the disc approaches the ideal constant-stress disc configuration.

$$F_d = \frac{\bar{\sigma}_{\theta,corr}}{\sigma_\theta^{max}} \tag{15}$$

where $\bar{\sigma}_{\theta,corr}$ is the corrected tangential stress, taking eccentric holes into consideration, thus defined as

$$\sigma_{\theta,corr} = \left(\frac{A}{A^*}\right)\bar{\sigma_\theta}, \qquad A^* = (gross\ area) - (bolt\ hole\ area) \tag{16}$$

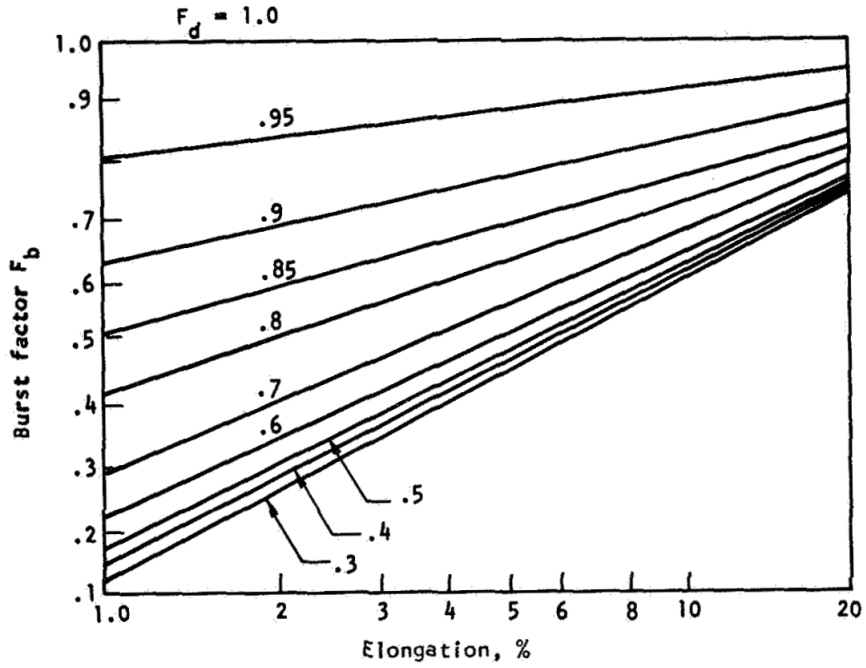

Figure 2.4: Disc burst factor as a function of ductility and design factor F_d[6].

2.4.2 Hallinan criteria

Hallinan burst criterion further builds upon Robinson criteria by introducing the ductility factor s[7], which is empirically derived and material dependent. The Hallinan burst criterion is defined as

$$BM_{Hallinan} = s \cdot \sqrt{\frac{\sigma_{UTS}}{\bar{\sigma}_\theta}} + (1-s) \cdot \sqrt{\frac{\sigma_{UTS}}{\sigma_\theta^{max}}} \tag{17}$$

Hallinan criteria takes material ductility into consideration, ductile metals will deforms and redistribute the peak stresses in the disc. This is favorable due to lower peak stresses resulting fewer defects and higher burst speeds. The ductility factor s is defined as

$$s = \frac{1}{NSR} \tag{18}$$

and where NSR stands for *Notched strength ratio*[8], and is defined as

$$NSR = \frac{\text{Strength of notched specimen}}{\text{UTS of smooth specimen}} \tag{19}$$

If $s < 1$ the metal is considered ductile an $s > 1$ it is considered brittle, if s is close to 1 it is considered to be somewhere in between, and thus reduced to Robinson's criteria.

2.4.3 Radial stress criteria

Radial stress criteria considers the average radial stress for a given cross-section at the radius r of the disc, and utilizes the maximum average radial stress to obtain the lowest burst margin.

$$BM_{Radial}(r) = \sqrt{\frac{\sigma_{UTS}}{\bar{\sigma}_r(r)}} \quad \Rightarrow \quad BM_{Radial} = \sqrt{\frac{\sigma_{UTS}}{\bar{\sigma}_r^{max}}} \tag{20}$$

Here $\bar{\sigma}_r^{max}$ denotes the average radial stress over the cross-section which generates the highest average radial stress.

NASA has further developed the radial stress criteria[6], applying the burst factor F_b also known as radial material utilization factor (RMUF) using empirical data.

$$BM_{Radial,NASA} = \sqrt{\frac{F_b \cdot \sigma_{UTS}}{\bar{\sigma}_r^{max}}} \tag{21}$$

2.4.4 Critical strain through cross-section criteria

The *critical strain trough cross-section criteria* suggest burst will occur when critical plastic strain has been reached through an arbitrary cross-section of the disc, which was utilized by *Y.A. Nozhnitsky* and *A.N. Servetnik*[9] when hazardous consequences of over-speed turbine rotors were considered. The critical plastic strain ϵ_c^p is defined as

$$\epsilon_c^p = ln(1 + \epsilon(\sigma_{UTS})) - \frac{\sigma_{UTS}(1 + \epsilon(\sigma_{UTS}))}{E} \tag{22}$$

where $\epsilon(\sigma_{UTS})$ denotes the engineering strain at the ultimate engineering tensile stress σ_{UTS}. Therefore the criteria is defined as

$$\epsilon_e^p > \epsilon_c^p \tag{23}$$

where ϵ_e^p denotes the plastic strain element wise.

2.4.5 Rice & Tracey failure criterion

Strain based Rice & Tracey criterion takes triaxiality stress state into consideration using ultimate and Von Mises strain values[10]. The criteria is defined as

$$BM_{R\&T} = \frac{\epsilon_c^p}{\epsilon_{R\&T}} \tag{24}$$

where ϵ_c^p is the critical plastic strain and

$$\epsilon_{R\&T} = \epsilon_{eqv.pl} \cdot R \tag{25}$$

here ϵ_c^p is the critical plastic strain, see Eqn. (22), $\epsilon_{eqv.pl}$ denotes the equivalent plastic strain and R is defined as

$$\frac{\sigma_H}{\sigma_{eq}} > \frac{1}{3} \Rightarrow R = exp\Big[0.5(3 \cdot \frac{\sigma_H}{\sigma_{eq}} - 1)\Big], \qquad \frac{\sigma_H}{\sigma_{eq}} \leqslant \frac{1}{3} \Rightarrow R = 1, \tag{26}$$

were σ_H and σ_{eq} denotes the hydrostatic and equivalent stress, respectively.

3 Methodology

The chapter presents the workflow throughout the project, starting with a general literature study.

3.1 Literature study

A literature study was performed with the ambition to get up to speed with industry standards, recent years development of different types of burst criteria, and the application of tensile test using structural analysis software. The search focused on turbine rotors and over-speed bursts of discs made of metal, mainly Inconel 718 alloy. Lund University library search engine *LUBsearch* was primarily used along with GKN Aerospace internal database.

3.2 Rotor material data

The turbine rotor was made of Inconel 718, and the raw material data used throughout the project was provided by GKN Aerospace Sweden. Previously the rotors were forged, but the turbine used in the experiment and analyzed in the thesis was produced by selective laser melting (SLM) additive manufacturing (AM) method with a 90° building direction, see Fig. 3.1.

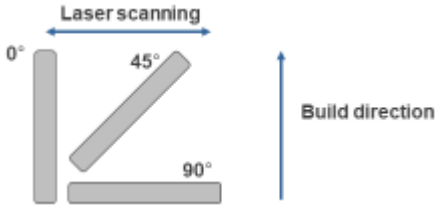

Figure 3.1: SLM additive manufacturing direction.

3.2.1 Experimental tensile tests

The material data was extracted from performing tensile tests on mechanical test specimens. Usually, the mechanical test specimens are printed along with the turbine rotor, allowing tensile tests to be manufactured with the same material batch as the rotor. This would ensure more accurate material data but was not performed in this case. Nine different mechanical test specimen was printed in two different batches. Three specimens were printed in the first batch at 0°, referred to as specimens 11, 12, and 13. The last six specimens were printed simultaneously, three at 0° referred to as specimens 30, 31, and 32, the rest were printed at 90° referred to as specimen 35, 36 and 37. When performing the tensile experiment, the gauge length was four times the size of the diameter of the tensile test specimen.

Figure 3.2: Tensile tested specimens produced using SLM additive manufacturing method.

3.2.2 Hockett Sherby Hardening law

The Hockett Sherby constants, see Eq. (10), were extracted using the tensile test data from the nine specimens. Preparation of the data was performed by converting the engineering stress-strain points to true stress-strain, see Eq. (7). Moreover, The inelastic strain was calculated for each data point, see Eq. (11), and data points below 0.03% inelastic strain were removed due to noise and large stress deviations between specimens. Finally, the data is truncated, a common practice is to truncate the data to 8% engineering strain, but due to performing failure simulations the truncation was extended to the UTS strain.

Excel 2016 was used to perform the curve fitting using the Hockett Sherby equation. Using the "SUMXMY2" function, see Eq. (27) to calculate the sum of squares, were the constants A, B, m, and n, see Eq. (10), were optimized to minimize the sum of squares using Excel 2016 Add-on Solver with the GRG Nonlinear solver method.

$$SUMXMY2 = \sum_{e=1}^{n} (\sigma_t^e - \sigma_{t,HS}^e)^2 \tag{27}$$

3.2.3 Average hardening model

The average hardening model was generated using the raw data point generated by the tensile tests of the nine specimens. The same preparation process was performed as for the Hockett Sherby method. Furthermore, all nine data sets were linearly interpolated with an increment of 0.05% strain using *Matlab R2017a*, generating an average stress-strain curve of the nine specimens. The average stress-strain curve was truncated when four out of the nine stress-strain curves had reached its true inelastic engineering ultimate tensile strength.

3.2.4 Implementation

The three material hardening models were implemented in *Engineering Data* tab in *ANSYS Mechanical 19.1* as *Multilinear Isotropic Hardening*. It should be noted that *ANSYS Mechanical 19.1* assumes perfect plastic behavior past the highest strain data point.

3.3 Preprocessing model

The model used to perform the structural analysis simulation using *ANSYS Mechanical 19.1* was developed by GKN Aerospace and simplified for simulation purposes. Dividing the turbine into 1/58 arc sections, including a single blade to reduce the computing time, see Fig. 3.3.

3.3.1 Mesh and mesh dependency

The mesh used to perform the prestudy was developed by *GKN Aerospace Sweden* seen in Appendix A, this mesh will be used as a reference, for comparison. The mesh developed for this project was made in *ANSYS mechanical 19.1* by adding *Automatic Method* with standard settings along with *Face Sizing* to all fillets in the blade area with the *Element Size* set to $0.9mm$. Furthermore, *Nonlinear Mechanical* was set as *Physical Preference* under *Details of "Mesh"* to better facilitate the nonlinear plastic behavior. *Max Size* was set to $0.0012mm$ for element sizes below or equal to $0.0012mm$, else it was equal to the element size to limit the spread element sizes. *Element Size* was also adjusted to find a suitable compromise for accuracy and computing time. Elastic simulations were performed for several mesh sizes at $\omega = \omega_{Burst}^{Exp}$ until convergence was reached for maximum equivalent stress of disc section. Afterward, elasto-plastic simulations were performed at $\omega = \omega_{Burst}^{Exp} \cdot 0.96862$ to validate the mesh dependency against elasto-plastic simulations.

3.4 Static structural analysis

All the simulations were made using *Static Structural* module in *ANSYS Workbench 19.1*. The material data was implemented by filling out the data sheets in *Engineering Data*. Temperature changes were not considered so the *Thermal Strain Effects* was set to *No* under *Material* in *Geometry* but the reference temperature was set to $293.15K$ ($20°C$). Cylindrical coordinate system were imported under *Coordinate systems* and *Cyclic Region* was set after importing *Symmetry*. *Standard Earth Gravity*, *Rotational Velocity*, *Fixed Support* were added, see Fig. 3.4. Moreover, *Commands (APDL)* were added under *Solutions* to run the burst margin evaluation scripts after the structural simulations were performed. Finally, the results are normalized separately, therefore the elastic- and elasto-plastic simulation results are not correlated.

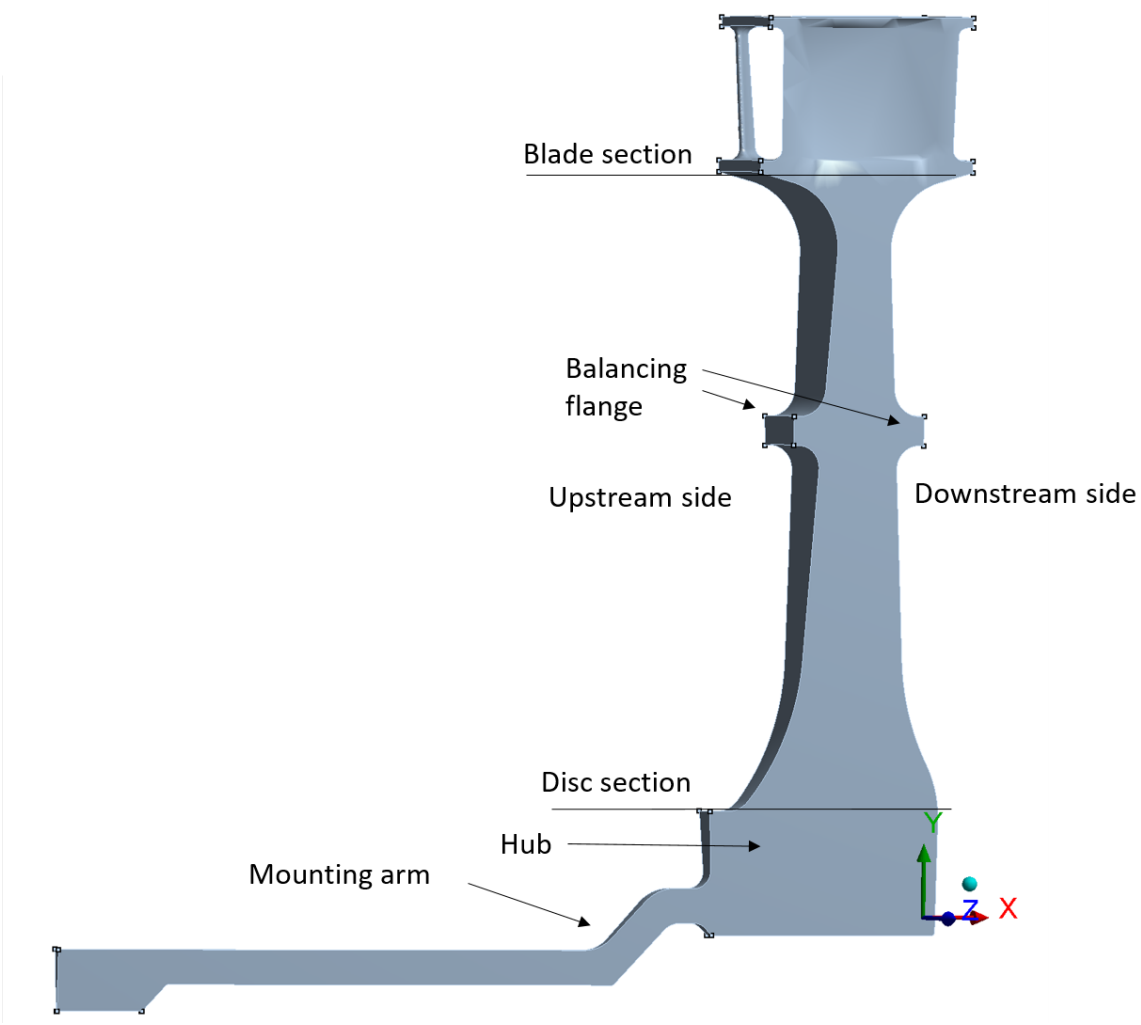

Figure 3.3: 1/58th arc section of the rotor model.

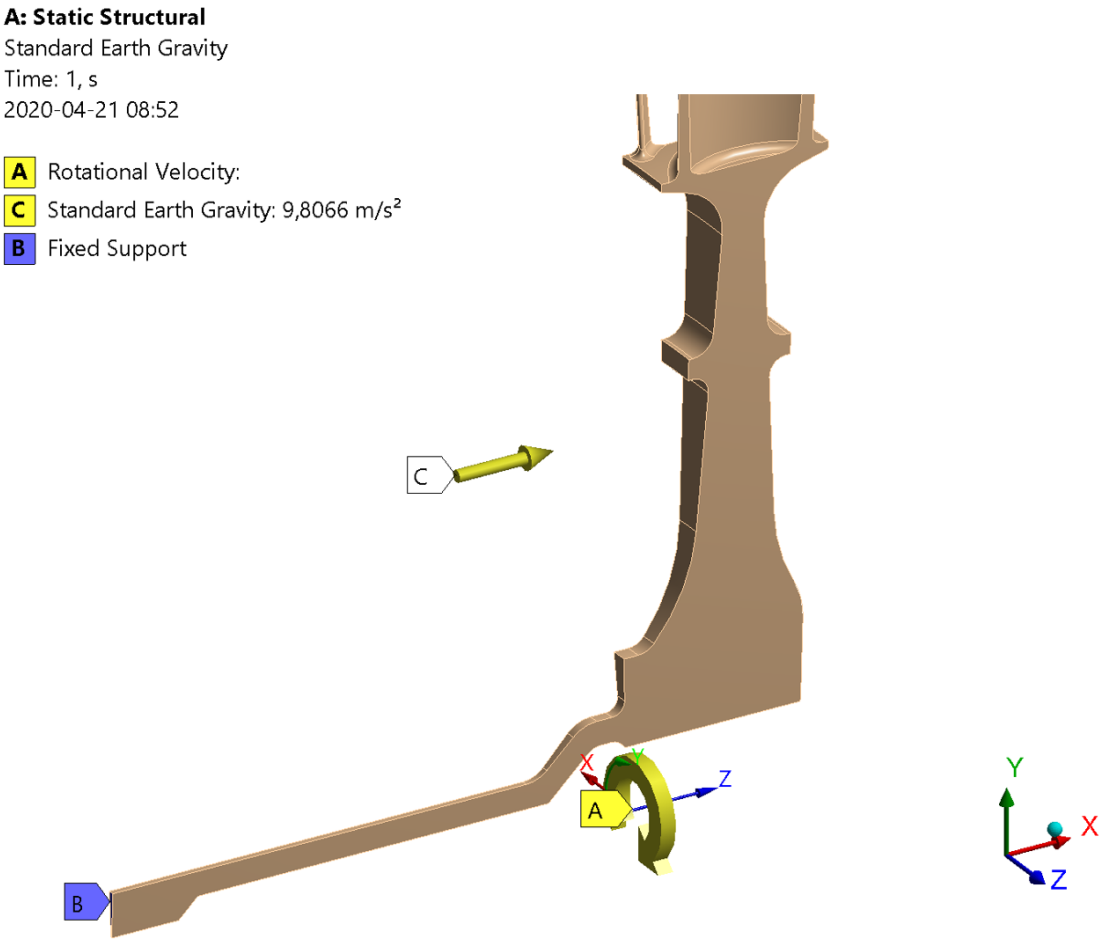

Figure 3.4: Boundary conditions and loads applied during *static structural analysis*.

Load step	norm. Rotational velocity $(\omega/\omega_{Burst}^{Exp})$[-]
1	0.48431
2	0.72646
3	0.89597
4	0.96862
5	0.98072
6	0.99283
7	0.99404
8	0.99525
9	0.99646
10	0.99768
11	0.99889
12	1.00010
13	1.00131
14	1.00252
15	1.00373
16	1.00494

Table 3.1: Normalized rotational velocity load steps used for *Static Structural Analysis*, normalized with respect to experimental burst speed.

3.4.1 Elasto-plastic analysis

All hardening laws were implemented using *Multilinear Isotropic Hardening* with increments of 0.05% strain. Table 3.1 presents the load steps applied when performing the elasto-plastic simulation. *Nonlinear Effects* was set to *Yes* and *Large Defection* was set to *On* under *Analysis Settings*. The elasto-plastic simulations ran until convergence could not be achieved.

3.5 Implementation of Fracture criteria

The fracture criteria were only applied for the disc section, see Fig. 3.5, utilizing *Commands (APDL)* implemented under *Solution* which executes *APDL* code. Visualization diagrams and figures was generated using *ANSYS Mechanical 19.1* and *Matlab R2017a*.

Area weighted mean hoop stress criteria and the *Hallinan criteria* with and without the burst factor proposed by NASA were calculated using plain *"get"* commands in (APDL) code and applying the equations, see Eqs. (12), (14) and (17). Furthermore, the radial stress had to be calculated for each layer of elements radially, see Eq. (20), to obtain the minimal radial burst margin. Moreover, the *critical plastic strain through cross-section* criteria and Rice & Tracey failure criteria were calculate using *MATLAB R2017a* by exporting the required element parameters from *ANSYS mechanical 19.1*

and applying Eq. (24) & (22).

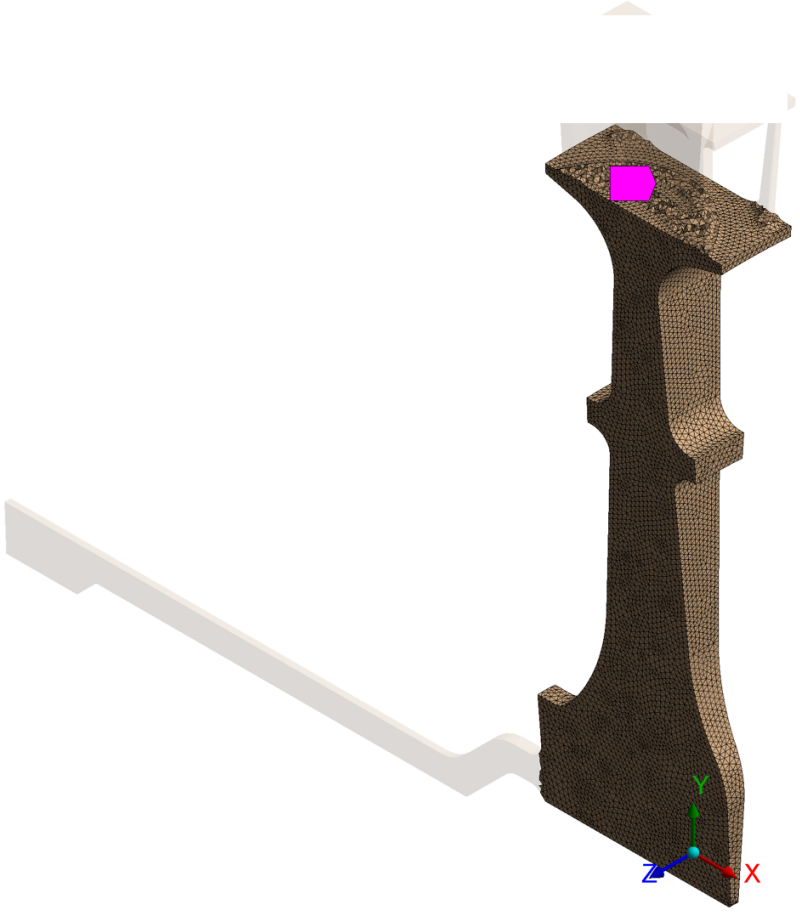

Figure 3.5: Disc section selected, the elements which fracture criteria were applied on.

4 Results

4.1 Mesh dependency study

Reducing the average element size incrementally until maximum equivalent stress in the disc section converged using linear elastic simulations allowed the mesh dependency against linear elastic simulations to be observed. Furthermore, performing the same analysis using elasto-plastic simulations until the maximum plastic strain converged allowed the mesh dependant against plastic simulations to be observed. In Fig. 4.1 one can see how the curves flatten out with an increasing number of nodes. The dotted red line indicates the mesh which was selected, resulting in approximately 300000 nodes and 200000 *"Tet10"* elements. This is a reduction from the prestudy-mesh by approximately 174400 nodes and 120000 elements.

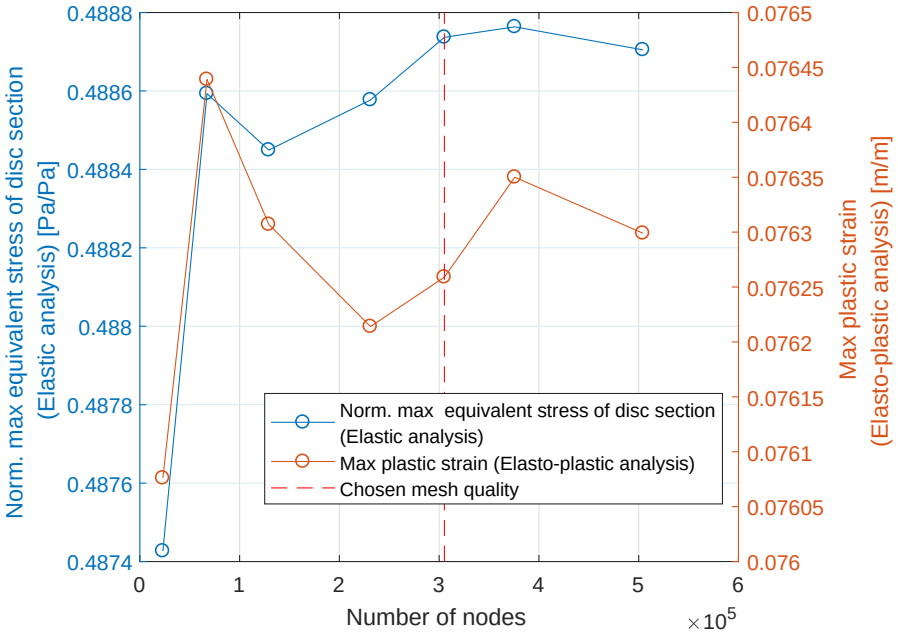

Figure 4.1: Norm. maximum σ_{eqv} using elastic simulations and maximum plastic strain using elasto-plastic simulations with respect to number of nodes, evaluate mesh dependency in the disc section.

4.2 Material hardening model

Note that both axes in the hardening model figure 4.2 are normalized due to intellectual property rights held by *GKN Aerospace*. The Hockett Sherby hardening law (H-S) was applied using nine mechanical tensile test denoted 11-13 *(blue)*, 30-32 *(red)* and 35-37 *(orange)*, see Fig. 4.2. 30-32 *(red)* and 35-37 *(orange)* specimens were from the same batch and therefore more relevant to compare. 11-13 *(blue)* and 35-37 *(orange)* specimens were printed parallel to the pulling direction (0°), see Fig. 3.1.

One can note from Fig. 4.2 the superior tensile strength of the specimen printed at 90°, perpendicular to the building direction.

The (H-S) hardening curve truncated at 8% strain *(purple)* overestimates the stiffness between $8 - 28\%$ true plastic strain and underestimates the true stress above 40% true plastic strain, when related to the nine tensile tests. Resulting in a very conservative prediction of the material strength above 40% true plastic strain, especially when considering large strains past 80%. Furthermore, the (H-S) hardening curve truncated at true ultimate tensile strength *(green)* overestimates the tensile strength of the material between $8 - 32\%$ true plastic strain and underestimates the tensile strength past 52% true plastic strain. Resulting in an overall good prediction, yet somewhat conservative past 52% true plastic strain. The average of all nine tensile tests truncated at UTS is displayed in *black*. Finally, the critical plastic strain was calculated using the average raw data from the nine tensile test specimen, resulting in a critical plastic strain of $\epsilon_c^p = 59.88$, this value has been normalized to stay consistent.

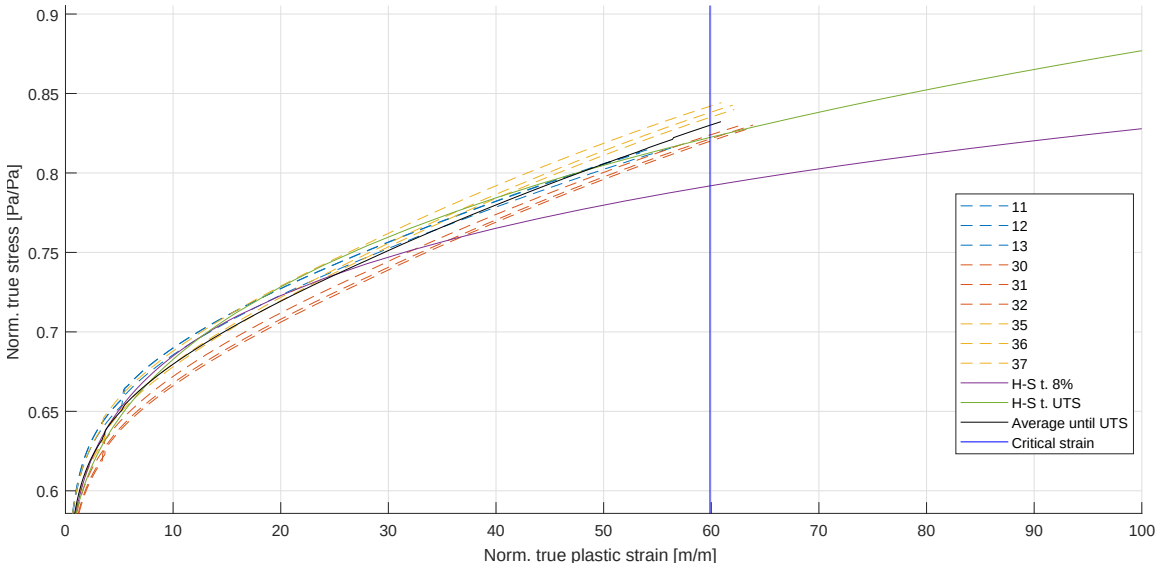

Figure 4.2: Normalized stress-strain curve with fitted hardening models onto experimental tensile tests . *(Red)* printed in 90° orientation, *(blue)* and *(orange)* printed in 0° orientation but printed in different batches.

4.3 Static structural analysis

The static structural analysis was performed using elastic and elasto-plastic properties. The linear elastic simulation was performed for $\omega = \omega_{burst}^{exp}$. The nonlinear elasto-plastic simulations were performed for all hardening models and controlled by stepwise increasing the rotational velocity, see Table 3.1, until excessive deformation was reached. The results have all been normalized against the maximum stress, which was achieved in the tangential direction (σ_θ), Fig. 4.3 for the linear simulation and

Fig. 4.7 for the elasto-plastic simulation. The normalization values used for the linear elastic and elasto-plastic simulation are not correlated.

4.3.1 Elastic analysis

Normalized tangential, radial, axial, and equivalent stress along with total deformation and strain contour plots for ω_{burst}^{exp} are presented in Fig. 4.3 & 4.4. Radial stress σ_r concentrations occur just below the balancing flange in the fillet and the tangential stress σ_θ concentration occurs on the edge of the hub, on the downstream side, which seems reasonable given the boundary condition in Fig. 3.4. The radial stress σ_r reaches a maximum of approximately 77%, and the axial stress σ_z reaches a maximum of 21.5% of the maximum tangential stress. The axial stress σ_z concentration occurs in the fillet between the upper disc and the blade.

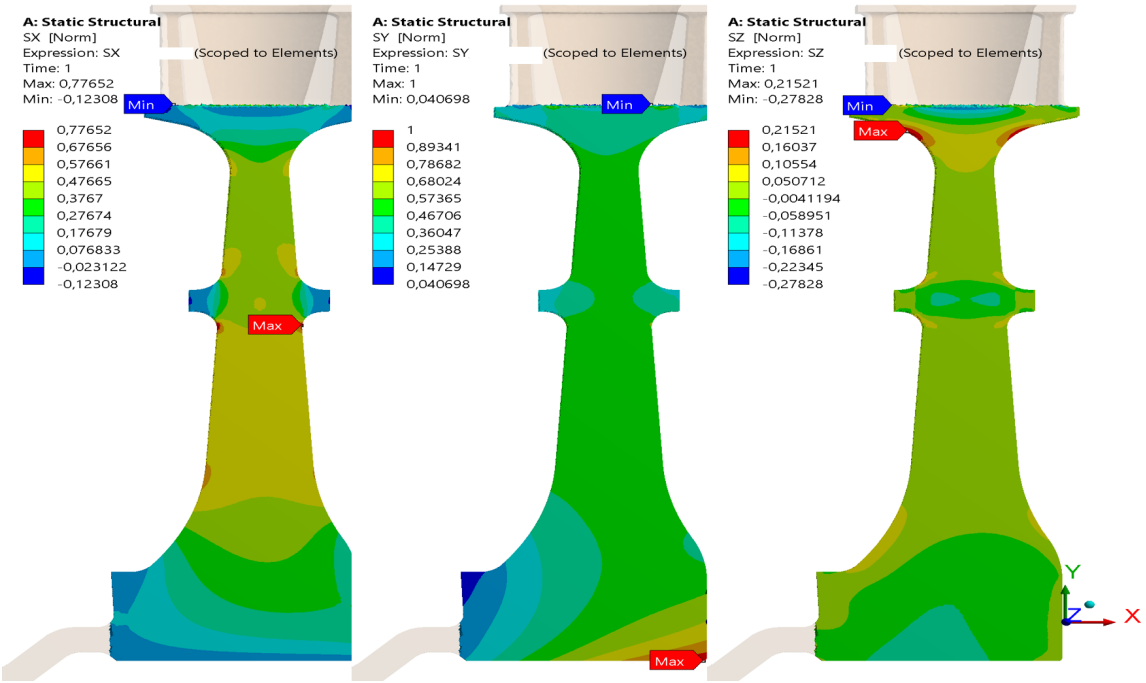

Figure 4.3: Normalized radial (σ_r), tangential (σ_θ) and axial (σ_z) contour stress plots from elastic analysis with $\omega = \omega_{burst}^{exp.}$.

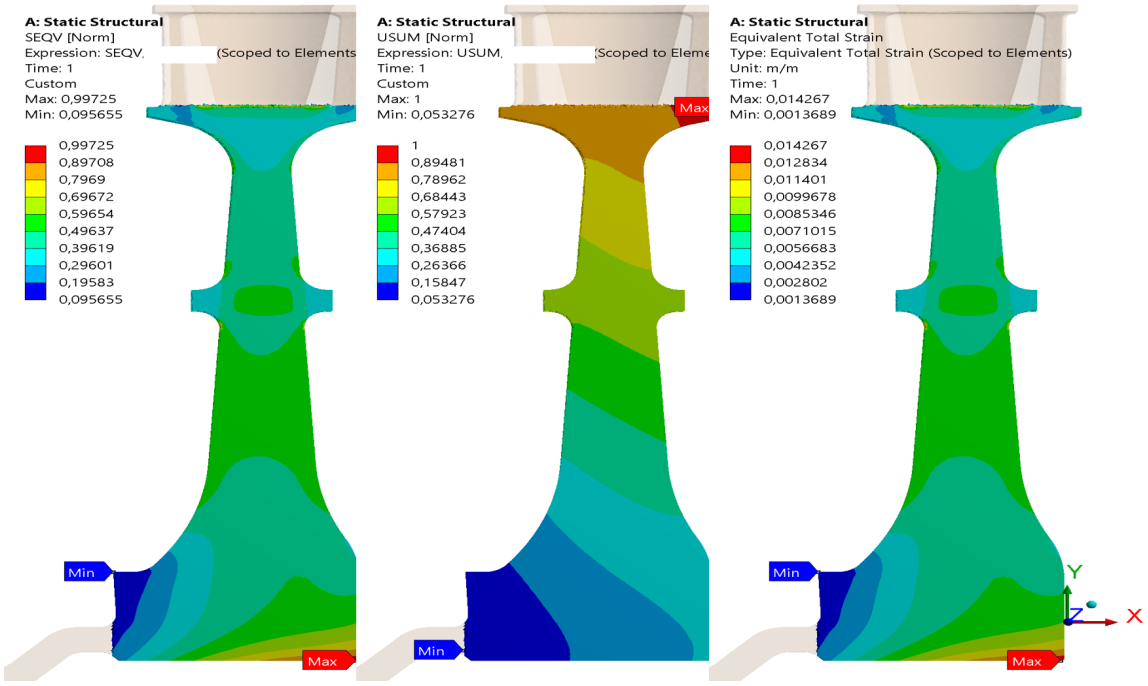

Figure 4.4: Normalized σ_{eqv}, normalized total deformation and total strain ϵ_{tot} contour plots from elastic analysis with $\omega = \omega_{burst}^{exp.}$.

4.3.2 Elasto-plastic analysis

The highest rotational velocity achieved at the last converged load step for each hardening model is presented in Table 4.1. The highest velocity was achieved by the H-S hardening model truncated at UTS, and second, came the average hardening model truncated at UTS.

The highest rotational velocity obtained from the elasto-plastic last converged load step correlate well with the experimental burst speed and did not vary much with different hardening models, see Table 4.1. $\omega_{H-S\,t.\,8\%}^{Num.\,max}$ and $\omega_{avg.\,t.\,UTS}^{Num.\,max}$ could not converge past the experimental burst speed, and thus underestimating the burst speed by -0.4746% and -0.2545%, respectively. Furthermore, the H-S hardening model truncated at UTS yielded the most accurate prediction, overestimated the burst speed by 0.2218%.

Hardening model	$\omega_{\mathbf{H-S\,t.\,8\%}}^{\mathbf{Num.\,max}}$	$\omega_{\mathbf{H-S\,t.\,UTS}}^{\mathbf{Num.\,max}}$	$\omega_{\mathbf{avg.\,t.\,UTS}}^{\mathbf{Num.\,max}}$
Rotational velocity of last converged load step	$0.995\omega_{burst}^{exp.}$	$1.002\omega_{burst}^{exp.}$	$0.997\omega_{burst}^{exp.}$

Table 4.1: Rotational velocity of last converged load step for each hardening model.

The normalized tangential, radial, axial, and equivalent stress along with total strain and deformation contour plots for all hardening models at $\omega = \omega^{Num.max}$ are presented in Fig. 4.5-4.10. Elasto-plastic contour plot displaying radial stress σ_r shows

how the stress concentration still occurs in the fillet just below the balancing flange but has expanded trough the whole lower part of the disc except for the hub section. The tangential stress σ_θ concentration occurs just below the blade section, on the downstream side of the hub propagating upward and small concentrations just above and below the balancing flange. The axial stress σ_z concentration occurs in the fillets leading down to the mounting arm by which the turbine is fixated. The inside fillet is subject to tensile stress, and the outside fillet is subject to compressive stress.

Comparing the different stress components, the tangential stress σ_θ is subject to the highest peak stress where radial stress σ_r and axial stress σ_z reach approximately 7% and 35% lower peak stresses, respectively. Furthermore, the total deformation plots gradually increase in deformation with radius, more so on the downstream side than on the upstream side. The maximum equivalent total strain occurs on the downstream side of the hub.

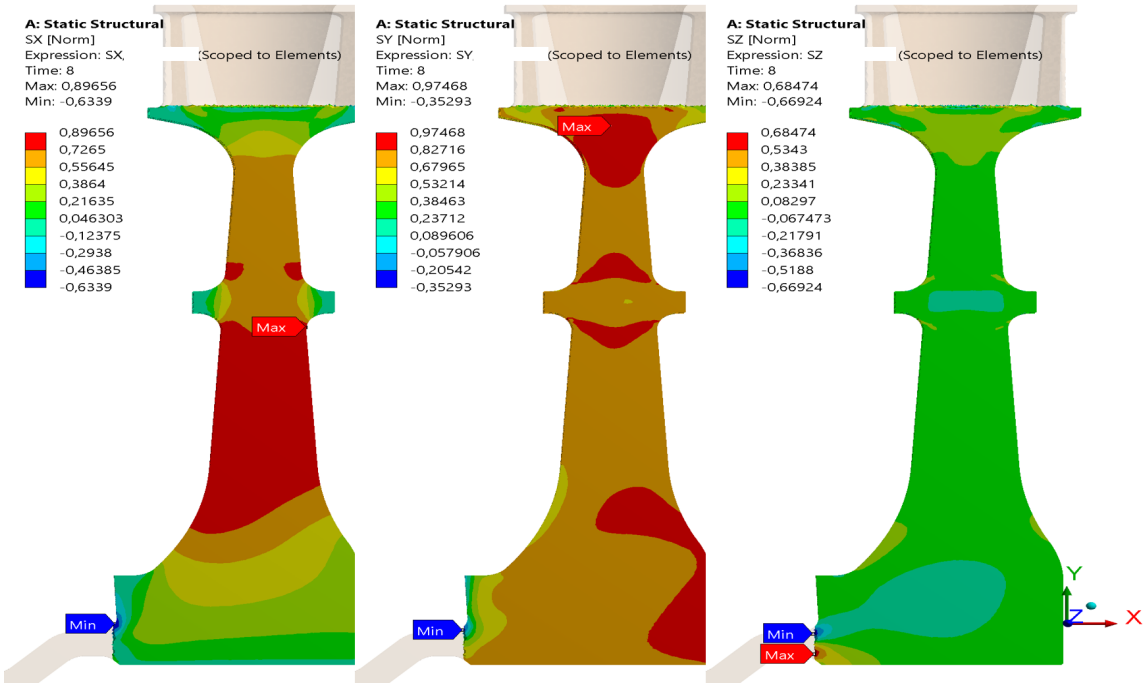

Figure 4.5: Normalized radial(σ_r), tangential (σ_θ) and axial (σ_z) contour stress plots from the elasto-plastic analysis using Hockett-Sherby hardening model truncated at 8% strain, $\omega = \omega_{H-S\,t.8\%}^{Num.max}$.

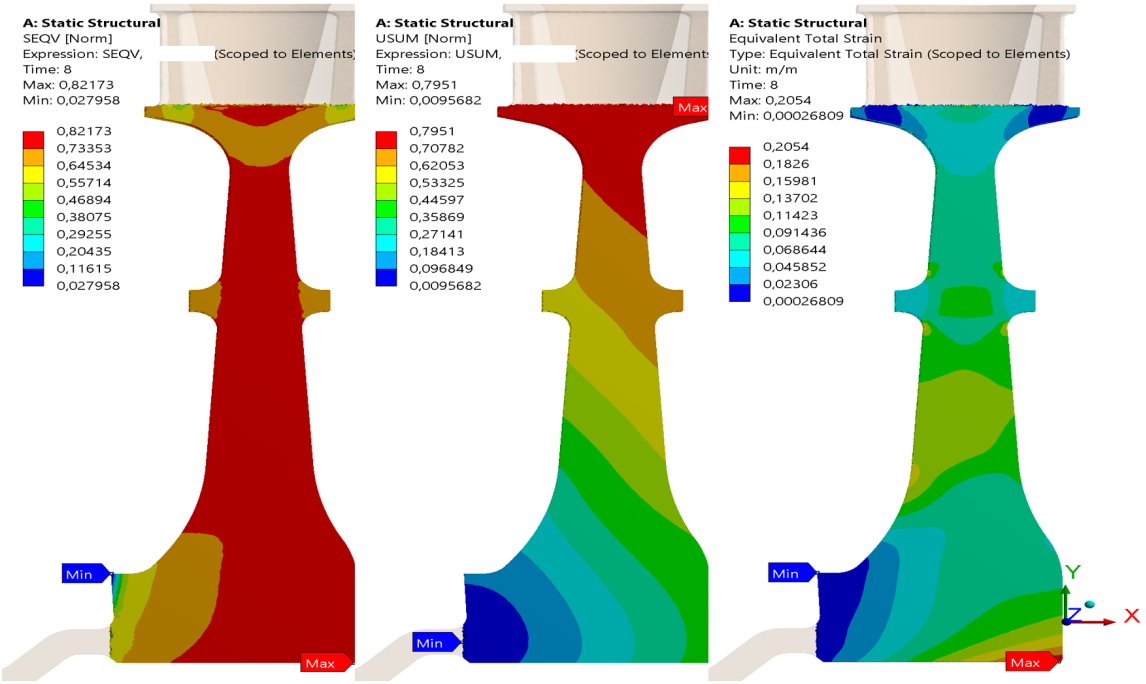

Figure 4.6: Normalized σ_{eqv}, normalized total deformation and total strain ϵ_{tot} contour from plots the elasto-plastic analysis using Hockett-Sherby hardening model truncated at 8% strain, $\omega = \omega^{Num.max}_{H-S\,t.\,8\%}$.

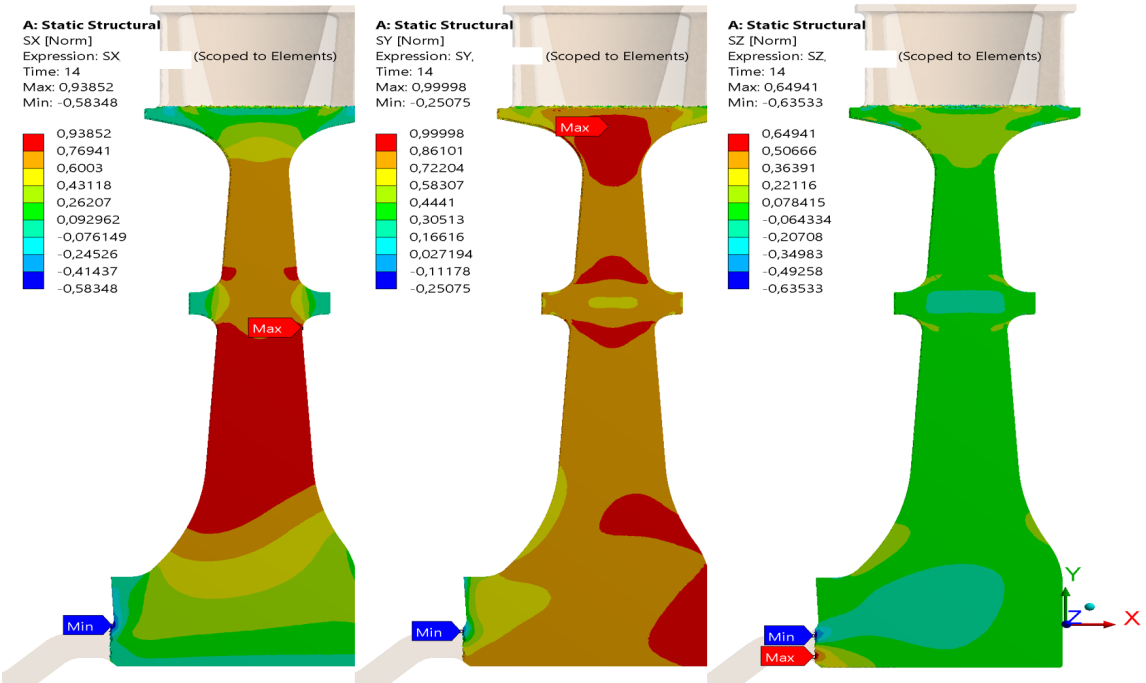

Figure 4.7: Normalized radial (σ_r), tangential (σ_θ) and axial (σ_z) contour stress plots from the elasto-plastic analysis using Hockett-Sherby hardening model truncated at UTS, $\omega = \omega^{Num.max}_{H-S\,t.\,max}$.

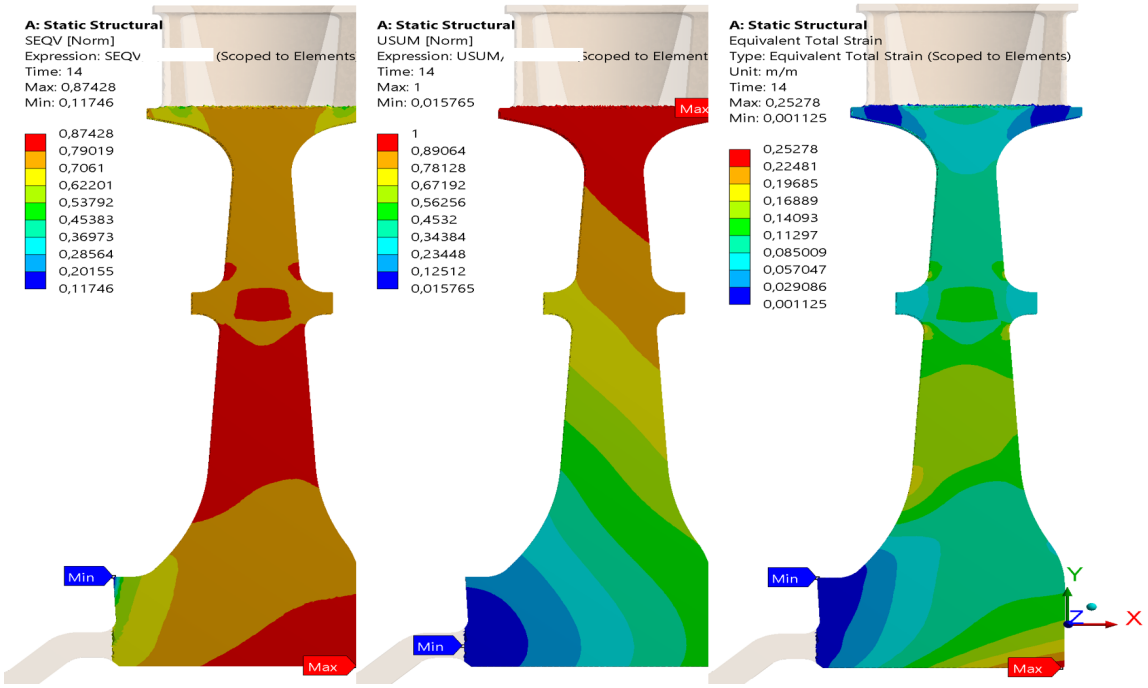

Figure 4.8: Normalized σ_{eqv}, normalized total deformation and total strain ϵ_{tot} contour plots from the elasto-plastic analysis using Hockett-Sherby hardening model truncated at UTS, $\omega = \omega^{Num.max}_{H-S\,t.\,UTS}$.

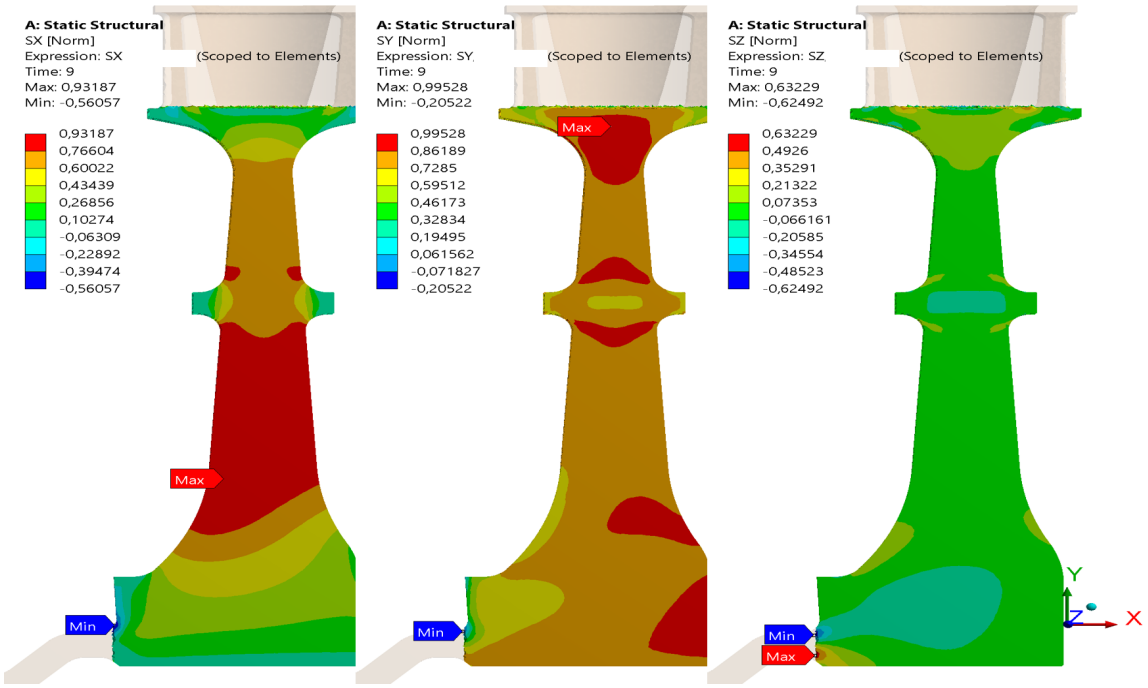

Figure 4.9: Normalized radial (σ_r), tangential (σ_θ) and axial (σ_z) contour stress plots from elasto-plastic analysis with $\omega = \omega^{Num.max}_{Avg.\,t.\,at\,UTS}$.

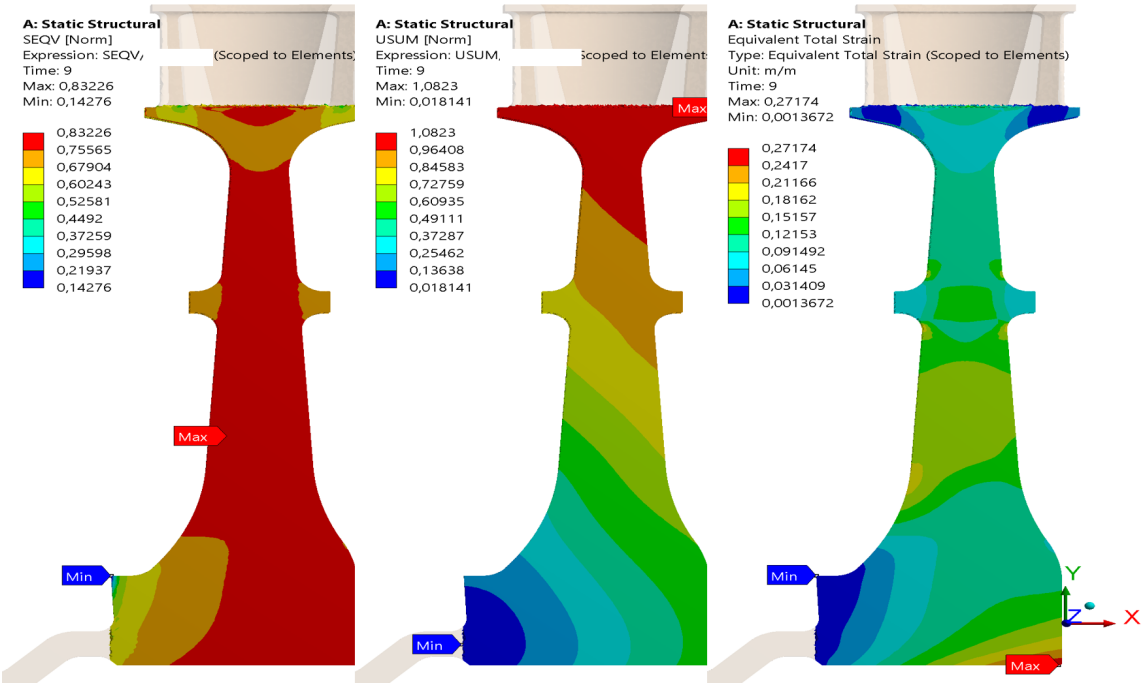

Figure 4.10: Normalized σ_{eqv}, normalized total deformation and total strain ϵ_{tot} contour plots from the elasto-plastic analysis with $\omega = \omega^{Num.max}_{Avg\,t.\,at\,UTS}$.

4.4 Fracture criteria

The *area weighted mean hoop stress*, *Hallinan* and *radial stress* burst margin criteria applied to linear elastic simulation results for $\omega = \omega^{exp}_{burst}$ are given in Table. 4.2. The *area weighted mean hoop stress criteria*, see Eq. (12) gave the most accurate prediction, overestimating the burst speed by 1.04%, the *radial criteria* underestimating the burst speed by 5.6% and the *Hallinan criteria*, see Eq. (17) was the least accurate, underestimating the burst speed by 11.7%. Furthermore, The NASA modification of the *area weighted mean hoop stress* and *radial criteria*, see Eq. (14) and (21), did not help the criteria to better predict the burst speed in this case.

The results regarding the burst factor F_b and the design factor F_d for the *area weighted mean hoop stress* and *radial stress* criteria will not be presented due to intellectual property rights held by *GKN Aerospace*.

The same burst margin criteria were applied to elasto-plastic simulation results for $\omega = \omega^{exp}_{burst}$ using all hardening models, see Table 4.3. For $\omega = \omega^{Num.max}$, all the burst margins give a conservative estimation of the burst speed, where the hardening model of H-S truncated at 8% strain gave overall the most accurate results. The other two hardening models, H-S and average truncated at UTS, delivered similar burst margins. Using the elasto-plastic simulation result, *area weighted mean hoop stress criteria* yielded the most accurate prediction, underestimating the burst margin by $5.1-6.6\%$. The *Hallinan* and *radial* criteria delivered similar results, which underestimated the

Elastic burst margin criteria	$\omega_{\mathbf{Burst}}^{\mathbf{Exp.}}$ (1.000)
(AWMHS)	1.0105
(AWMHS) NASA	0.9317
Hallinan	0.8828
Radial	0.9438
Radial NASA	0.8954

Table 4.2: Burst margin calculated using the linear elastic simulations

burst speed by $9.2 - 10\%$

Elastio-plastic burst margin criteria	$\omega = \omega^{\mathbf{Num.max}}$		
Hardening model	**H-S t. 8% strain (1.005)**	**H-S t. UTS (0.9978)**	**avg. t. UTS (1.003)**
(AWMHS)	0.9538	0.9365	0.9365
(AWMHS) NASA	0.8793	0.8634	0.8634
Hallinan	0.9129	0.8980	0.8986
Radial	0.9115	0.8910	0.8900
Radial NASA	0.8648	0.8452	0.8443

Table 4.3: Burst margin calculations from the elasto-plastic simulations using the three hardening models.

4.4.1 Critical strain trough cross-section criteria

Figure 4.11 - 4.13 shows the propagation of elements reaching critical plastic strain for the last three converged load steps for all material hardening models. The element-wise calculation was performed using Eq. (22). Only 0.27% of all elements discretizing the disc section, see Fig. 3.5, reached the critical plastic strain limit before convergence was lost when using the H-S hardening model truncated at 8% strain. The elements were located on the downstream side of the hub, see Fig. 4.11.

Furthermore, using the H-S hardening model truncated at UTS resulted in 5.47% of the disc section reached critical plastic strain rate until convergence was lost. From figure 4.12, it can be seen that the elements reaching critical plastic strain have not propagated trough the disc to fulfill the *critical strain trough cross-section criteria*. One can also note the incremental increase in elements reaching critical plastic strain located in the hub, on the downstream side, propagating slowly towards the upstream side. While the elements which have reached critical plastic strain located in the disc under the balancing flange propagate faster trough the disc.

Finally, for the average hardening model truncated at UTS , see Fig. 4.13, resulted in 15.28% of all the elements reaching critical plastic strain. Still, the elements located

in the corner hub propagate slowly. Again, the elements under the balancing flange on the disc reach critical plastic strain and propagate rapidly. Here the elements fulfilling the criteria managed to propagate trough the disc, fulfilling the burst criteria.

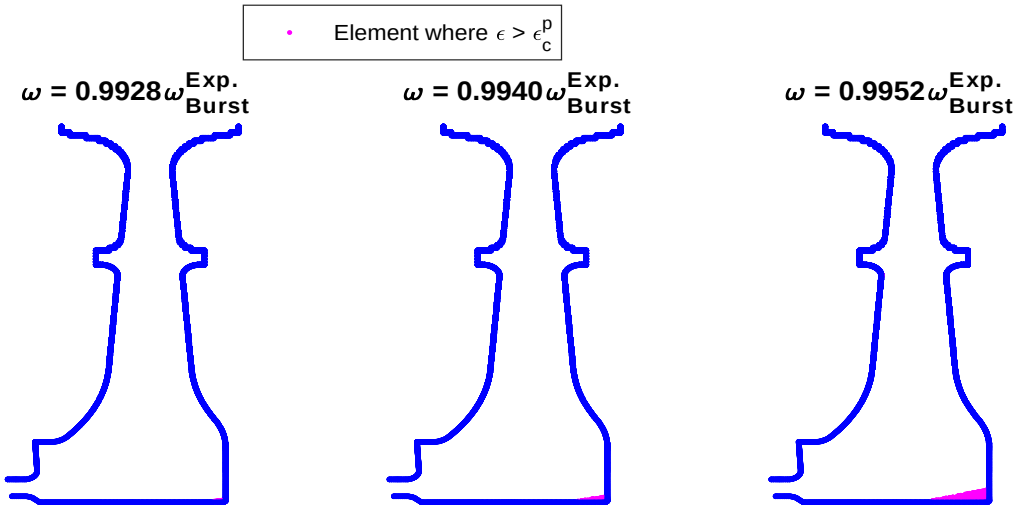

Figure 4.11: Elements past critical plastic strain, for the last three converged load steps, using Hockett Sherby truncation at 8% engineering strain.

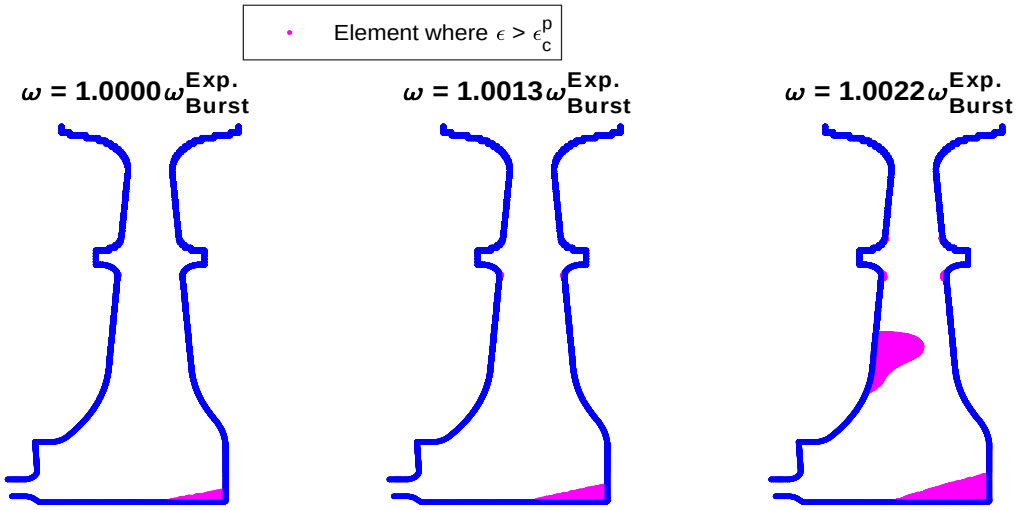

Figure 4.12: Elements past critical plastic strain, for the last three converged load steps, using Hockett Sherby truncation at true plastic UTS.

4.4.2 Rice & Tracey failure criteria

Figure 4.15 - 4.16 presents the propagation for the last converged load steps of Rice & Tracy *criteria* applied element-wise for all three material hardening models. The element-wise calculation was performed using Eq. (24). The propagation of elements

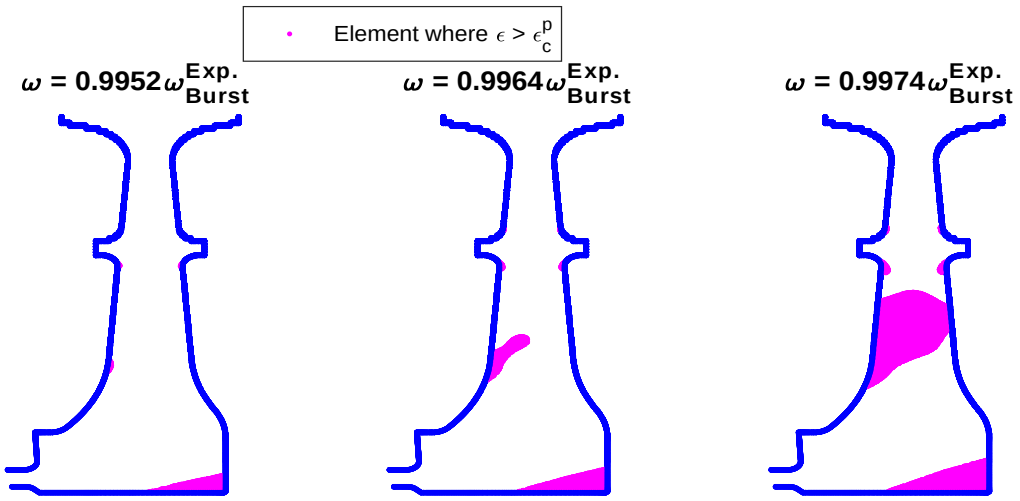

Figure 4.13: Elements past critical plastic strain, for the last three converged load steps, using the *averaged truncated at UTS* model.

reaching the R&T margin starts in the fillet between the hub and lower disc on the upstream side. Extending fully trough the disc to the downstream side and up to the balancing flange, when applying the H-S truncated at 8% strain hardening model, see Fig. 4.14. 24.8% of all elements defining the disc section, see Fig. 3.5 fulfilled the R&T criteria on the last converged load step. The elements located in the hub on the downstream side fulfill the R&T criteria but do not propagate fast with each load step.

Furthermore, applying the H-S hardening model truncated at UTS, more load steps converged, and higher rotational speed was achieved, resulting in a more dominant propagation of elements reaching the R&T criteria. 51.8% of all element discretizing the disc section passed the R&T criteria on the last converged load step. The propagation started in the fillet between the hub and disc on the upstream side and further extended through the disc towards the downstream side. Then continued to propagate towards the hub and balancing flange, passing the flange, and reaching the fillet leading up to the blade section, see Fig. 4.15. The elements located in the hub on the downstream side which fulfill the R&T criteria do not propagate as fast with each load step as the elements by the balancing flange.

Moreover, the number of elements reaching the R&T criteria for each load step, increased even further when using the average truncated at UTS hardening model. 58.5% of all elements defining the disc section reached the R&T criteria. This is evident through the aggressive propagation in which the elements pass the R&T criteria, see Fig. 4.16. The propagation starts in the fillet between the hub and disc on the upstream side, extending through to the downstream side and further propagating towards the hub and blade section.

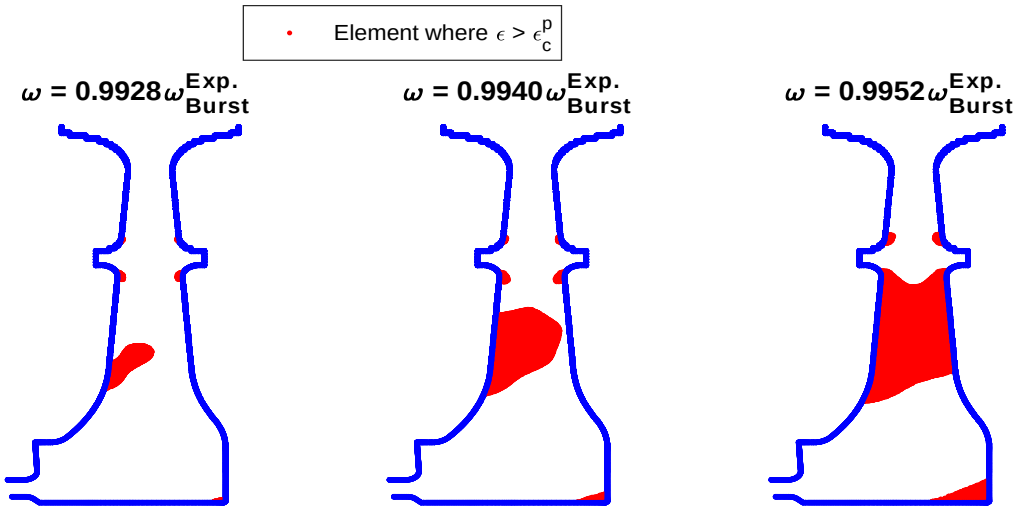

Figure 4.14: Rice & Tracey criteria applied element wise, for the last three converged load steps, using Hockett Sherby truncation at 8% engineering strain.

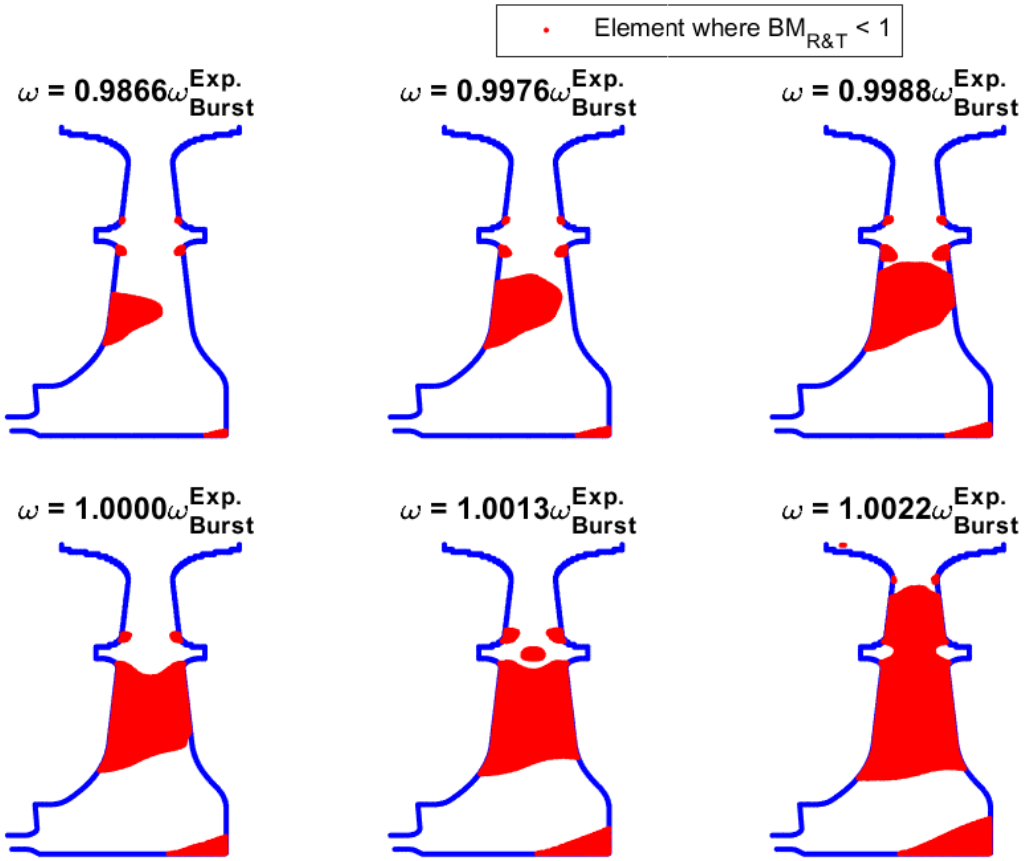

Figure 4.15: Rice & Tracey criteria applied element wise, for the last six converged load steps, using Hockett Sherby truncation at true plastic UTS.

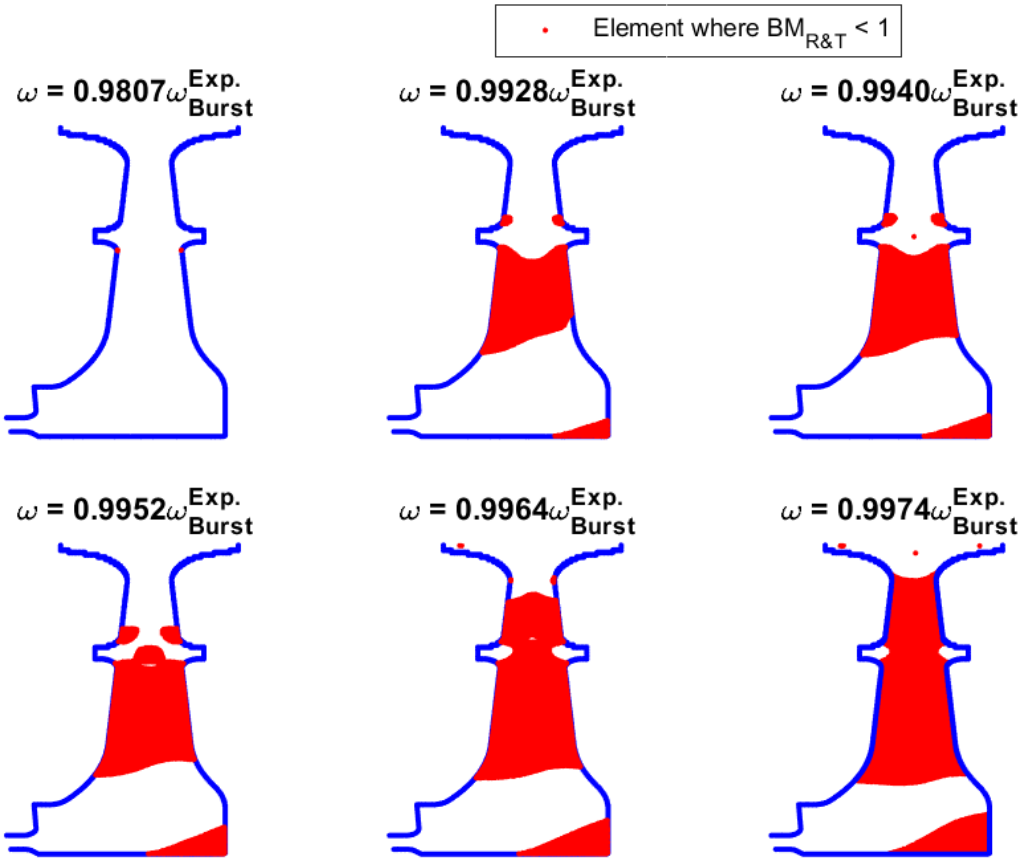

Figure 4.16: Rice & Tracey criteria applied element wise, for the last six converged load steps, using the *averaged truncated at UTS* model.

5 Discussion

5.1 Mesh dependency study

The mesh dependency was performed by incrementally decreasing overall element size. Which is the general idea of measuring the information loss due to mesh quality, thus trying to eliminate it. The number of nodes and elements were reduced by approximately 37%, to approximately 300000 nodes and 200000 elements, yet matching the accuracy of the previous mesh. The chosen mesh was the sweet spot between accuracy and computational time. One could further improve the mesh, to reduce the computational time by trying different types of elements and mesh settings.

5.2 Material and hardening model

H-S hardening model truncated at 8% strain, see Fig. 4.2 *(purple)* overestimates the stiffness a small amount between $8 - 28\%$ true plastic strain and then underestimates the stiffness past 40% true strain. The model is very conservative past 40% true strain, which is troublesome when performing failure and burst simulations where large strains occur. Furthermore, the H-S hardening model truncated at UTS, see Fig. 4.2 *(green)*, overestimates the stiffness a small amount between $8 - 32\%$ true plastic strain. The true stress past 72% true plastic strain is a concern because the stiffness was not archived by the tensile test specimen. The model describes the hardening phase more accurately than when truncated at 8% strain, which is expected given the larger amount of data provided and is, therefore, a better choice for predicting burst compared to when truncated at 8% strain, but uncertainties lay past 72% true plastic strain. Finally, The average hardening model truncated at UTS was calculated by taking the average of the nine tensile test results. The curve follows the path of the nine tensile tests perfectly, as expected, see Fig 4.2 *(black)*.

The method to produce the H-S hardening models truncated at 8% strain are heavily tested and documented by *GKN aerospace*. When reconstructing the H-S hardening model truncated at 8% strain, there was a small difference in stiffness, by approximately -1.3% compared to the results produced by *GKN Aerospace*. Given the error, H-S truncated at UTS was made using the same method.

For future burst simulations, I recommend a more considerable amount of tensile test specimens manufactured simultaneously with the rotor and the measurement of dynamic elastic modulus for a more accurate interpretation of the elastic modulus.

5.3 Static structural analysis

Overall the results gained from the simulations using *ANSYS mechanical 19.1* have high credibility and are trustworthy. Very similar results have been achieved internally by *GKN Aerospace*. To further increase the accuracy and precision of the simulation results, the model should be a perfect replica of the burst tested one. Modeling the

manufacturing tolerance scatter, and no simplifications such as symmetry and filled blades should be included. Furthermore, the thermal effect could also be included modeling the temperature increase due to plastic deformation, and spin softening could also be investigated. The experiment was performed in a pressure vessel partially vacuumized, making it hard to model the magnitude of air resistance. Finally, one could test different yield criteria, which takes the triaxial stress state into account.

5.3.1 Elastic analysis

The highest stress was located in the tangential direction (σ_θ) on the lower part of the hub towards the downstream side, which was followed by radial stress (σ_r), where the highest radial stress was achieved just under the balancing flange located in the middle of the disc. The radial stress reached a stress magnitude of 77% that of the maximum tangential stress. Finally, the axial stress (σ_z) reached its maximum in the fillet between the blade and disc, reaching a magnitude of 21.5% compared to the maximum tangential stress, See Fig. 4.3. Furthermore, the total deformation, see Fig. 4.4 is gradually increasing with radius, which is expected given the nature of centripetal forces. The results attained were expected. The location and magnitude of the peak stresses correlate well with the pre-study. The proportions between the different stresses correlate well with the analytical equation of tangential stress described in [11].

5.3.2 Elasto-plastic analysis

The highest velocity was achieved using the H-S hardening model truncated at UTS, which is expected when observing Fig. 4.2, where the peak stress is much higher than the other hardening models. Note that the rotational velocity surpassed the experimental burst speed, which might be due to the overestimated strength past 72% true plastic strain. The model also surpasses the strength of the experimental tensile test by some margin. Furthermore, H-S truncated at UTS last converged load step yielded the most accurate rotational velocity, overestimating the experimental burst speed by 0.2218%. Furthermore, the second-highest velocity was achieved using the average hardening model truncated at UTS, which was not expected due to the lower peak strength in the stress-strain curve, see Fig. 4.2, relative to the H-S truncated at 8% strain. The model underestimated the experimental burst speed by 0.2545%. Finally, the H-S hardening model truncated at 8% strain underestimated the experimental burst speed by -0.4746% which was not expected due to profoundly conservative material stiffness.

The three given hardening models yielded a maximum rotational velocity spread of less than 1%. *ANSYS Mechanical 19.1* automatically made sub-steps between the different load steps, when convergence was hard to reach, making the last few sub-step increments very small. The results also correlated well to previously performed simulations by *GKN Aerospace*, which used the same turbine model and was performed using a reliable and well-tested method developed by *GKN Aerospace*. Therefore I

consider the method to perform the elasto-plastic analysis and the results to be valid.

The highest stresses were located in the tangential direction (σ_θ), just below the wing, see Fig. 4.7. The radial stress (σ_r) concentrated below the balancing flange and above the hub. The maximum radial peak stress was located in the flange between the bottom part of the disc and balancing flange on the upstream side, reaching a magnitude of 93.8% relative to the peak tangential stress. Lastly, the axial stress (σ_z) concentration occurred in the fillet on the mounting arm to which the turbine is fixated, resulting in peak stress of 68% relative to the tangential peak stress. The magnitude differences in peak stresses between tangential, radial, and axial stress have been somewhat reduced compared to the linear simulation, which is expected when taking plasticity into account. Peak stresses are redistributed thanks to material ductility, allowing for more of the material to be loaded. Finally, Observing the contour plots seen in Fig. 4.5-4.10, the radial stress proved to be the most detrimental. Given how the whole cross-section from the upstream to downstream is loaded and considering the origin of initial burst seen in the experimental burst test results in Appendix B.

5.4 Fracture Criteria

Considering the result of the linear elastic simulations, and applying the burst margins, see Table 4.3, showed that the *area weighted mean hoop stress criteria* predicted the burst speed with the highest accuracy, overestimating the experimental burst speed by 1.04%. Furthermore, the second-most accurate burst margin was calculated using the *radial criteria*, underestimating the experimental burst speed by 5.6%. The NASA modification of the *area weighted mean hoop stress* and *radial criteria*, see Eq. (14) and (21), did not increase the accuracy of the criteria to predict the burst speed better. This is not what I expected, perhaps reevaluation of the burst factor F_b should be considered for turbines designed by *GKN Aerospace* and produced using AM. The Hallinan criterion, see Eq. (17), performed the worst, underestimating the burst speed by 11.7%. Which is unexpected when noting that the criteria are an evolution of the *area weighted mean hoop stress* criteria, taking ductility into consideration when performing elastic simulations.

Furthermore, applying the same burst margins to elasto-plastic simulations, see Table. 4.3, and comparing hardening models by observing the maximum velocities $\omega = \omega^{Num.\,max}$ see Table 4.1, H-S truncated at 8% strain yielded overall the most accurate predictions. Which is unexpected due to being the least accurate hardening model when trying to converge close to $\omega = \omega^{Exp.}_{Burst}$. It should be noted that the purpose of burst margins are to be applied to elastic simulations and obtain a general burst margin prediction in the early stages of the design process. The criteria with the highest burst margin accuracy were *area weighted mean hoop stress*, with an underestimation of $5.1 - 6.6\%$ depending on the hardening model. *Hallinan criteria* calculated the second-most accurate burst margin, underestimation of $9.2 - 10\%$ from the experimental burst speed. This is surprising, being that the *Hallinan criteria*

builds upon the *area weighted mean hoop stress* criteria and include the ductility factor $s = 0.6$. Perhaps the ductility factor value should be reevaluated. Furthermore, The NASA modification of the *area weighted mean hoop stress* and *radial criteria*, see Eq. (14) and (21), did not increase the accuracy of the criteria. This is not what I expected. Perhaps the burst factor F_b also needs to be reevaluated, perhaps calculated for the turbines developed by *GKN Aerospace* and manufactured using AM.

5.4.1 Critical strain trough cross-section criteria

Results from *critical strain trough cross-section criteria* was not of much use when trying to estimate the burst speed. The different hardening models converged up to their respective $\omega = \omega^{Num.\,max}$, due to the different stiffness characteristics, see 4.2. However, the critical plastic strain was calculated following Eq. (22), which is used for all hardening models. Thus the hardening model with the highest stiffness should have the highest percentage of elements reaching critical plastic strain, but that is not the case. One could argue that even tho the small load step increments, the slope of the more conservative H-S hardening model truncated at 8% strain could not manage the velocity increase. Thus failing to converge abruptly, resulting in fewer elements fulfilling the criteria. The average hardening model truncated at UTS attained a higher percentage of elements reaching critical plastic strain before convergence was lost, compared to H-S truncated at UTS.

The *critical strain trough cross-section criteria* show mainly two different locations where elements were reaching critical plastic strain. One could quickly note the difference in the propagation speed might be a factor to consider. The fast propagation of elements reaching critical plastic strain occurred above the flange between the hub and disc, on the upstream side. The same location was concluded to be in the area of the crack origin seen in Appendix B. This is promising for the criteria; perhaps it could be used to predict the location of fracture and burst. One should note that the criteria are heavily dependent on the critical plastic strain ϵ_c^p.

5.4.2 Rice & Tracey failure criteria

The Rice & Tracey criteria behave much like the *critical strain trough cross-section criteria* but more amplified, which can be noticed on the percentage of elements fulfilling the criteria. Elements that fulfill the *R&T* criteria originate from the fillet between the disk and hub, on the upstream side. Same location as the elements fulfilling *critical strain trough cross-section criteria*, see Fig. 4.13 and 4.16. This is expected due to the element-wise strain dependency, which both criteria contain, see Eq. (23) & (24). The propagation of elements fulfilling the criteria extend further through the disk to the downstream side with increased speed, very similar to the *critical strain trough cross-section criteria*.

From the experimental burst test, see Appendix B, there is evidence that the first failure occurred on the upstream side just above the fillet between the hub and disc section. This is also supported by observing the *R&T* criteria plots shown in Fig. 4.14

- 4.16. The question then arises why did not the corner hub on the downstream side fail, where elements also fulfill the $R\&T$ criteria. One could argue that the propagation of elements fulfilling the criteria by the fillet spreads faster. Therefore the origin of the fracture can be pinpointed. Perhaps more tests are required to validate this claim.

The results are consistent throughout all the hardening models, and the position of elements fulfilling the criteria does correlate with the stress contour plots in Fig. 4.5 - 4.10. Furthermore, the usage of critical plastic strain must be said to be an uncertainty. There is not a lot that supports the reason for using critical plastic strain as done in Eq. (22) when calculating the $R\&T$ and *critical strain trough cross-section* criteria. Due to the critical plastic strain being a scalar and base upon tensile test specimens, many have found other parameters such as the Lode parameter and effective plastic strain to be useful [12] [13].

6 Conclusions

Given the small spread in maximum rotational velocity between the three hardening models being less than 1%, it is still of great importance to apply a precise hardening curve to predict burst accurately. Even more so when considering the high rotational velocities rotors achieve and the high safety margins used in the space industry. The H-S truncated at 8% strain proved to be too conservative and carries a significant safety factor, see 4.2. Therefore the hardening model is not suitable for burst and failure simulation. The evidence is also visible in the application of the $R\&T$ and *critical strain trough cross-section* criteria, where the information from H-S truncated at 8% strain is minimal compared to the H-S and average hardening models truncated at UTS.

The elastic analysis for its hasty computing provides unexpectedly accurate burst margin estimation, see Table 4.2. The *area weighted mean hoop stress* criteria without the NASA modification proved to be to most accurate of the bust margins by far, with an error of +1.04%. This method provides a good and quick estimation, usable during the design phase, when several models are compared. It also excludes the labor-intensive hardening model application and the high computational time required for performing elasto-plastic simulations. Furthermore, elasto-plastic simulations yielded the most accurate burst speed estimation by incrementally increasing the rotational velocity until convergence was lost. Between three hardening models, the maximum velocity achieved were between $0.9978 - 1.005\omega_{burst}^{exp.}$.

The *critical strain trough cross-section* did not estimate burst speed well, perhaps a more thorough analysis of the critical strain estimation should be performed. Moreover, the $R\&T$ criteria correlated well with the assumed initial burst location attained from the experimental burst test. It should be noted that there are indications that point towards how fast propagation of elements fulfilling the criteria develops correlate with where failure will occur.

To summarize, during the design phase, the linear elastic burst margins yield good results that are able to evaluate the model and ensuring that the safety margin is fulfilled. Furthermore, performing elasto-plastic simulation using the H-S or average hardening model truncated at UTS and successively increasing the rotational velocity until convergence was lost due to excessive deformation yields very accurate burst speed. Finally, applying the Rice % Tracy criteria element-wise and observing the propagation speed of elements fulfilling the criteria one could pinpoint the initial fracture origin.

References

[1] N. S. Ottosen and M. Ristinmaa, *The Mechanics of Constitutive Modeling*. Elsevier, 2005.

[2] P. Kelly, "Mechanics lecture notes: An introduction to solid mechanics." `http://homepages.engineering.auckland.ac.nz/~pkel015/SolidMechanicsBooks/index.html`, March 2020. Accessed on 2020-03-24.

[3] Y. Ling, "Uniaxial true stress-strain after necking," *AMP Journal of technology, Vol.5 No.1, pp.37-48*, 1996.

[4] J. Hockett and O. Sherby, "Large strain deformation of polycrystalline metals at low homologous tmeperatures," *Journal of the Mechanics and Physics of Solids*, vol. 23, issue 2, pp. 87–98, 1975.

[5] E. Robinson, "An improved turbine disk design to increase reliability of aircraft jet engines," *Trans. ASME Appl. Mech. Sect. 66, pp. 380*, 1944.

[6] U. S. NASA Lewis Research Center; Cleveland, OH, "Liquid rocket engine turbines, nasa-sp-8110," 1974.

[7] W. Barack and P. Domas, "An improved turbine disk design to increase reliability of aircraft jet engines," 1976.

[8] D. Porter and T. Totemeier, *Mechanical properties of metals and alloys*, p. 81. 2004.

[9] Y. A. Nozhnitsky and A. N. Servetnik, "Prevention of hazardous failure of the turbine rotor due to its overspeed," *IOP Conf. Series: Materials Science and Engineering 449*, 2018.

[10] J. R. Rice and D. M. Tracey, "On the ductile enlargement of voids in triaxial stress fields," *Journal of the Mechanics and Physics of Solids, 17, pp. 201-217*, 1969.

[11] A. M. Zenkour and D. S. Mashat, "Stress function of a rotating variable-thickness annular disk using exact and numerical methods," *Engineering, Scientific Research, 3, pp. 422-430*, 2011.

[12] Y. Bai and T. Wierzbicki, "A new model of metal plasticity and fracture with pressure and lode dependence," *International Journal of Plasticity 24, pp. 1071–1096*, 2008.

[13] A. Neimitz, J. Galkiewicz, S. Lipiec, and I. Dzioba, "Estimation of the onset of crack growth in ductile materials," *Materials 2018, 11(10)*, 2016.

Appendices

A Design of rotor for burst test

The following report is a limited summery of the experimental burst test prestudy, *Design of rotor for burst test* (DB042878). It was performed before the SLM additive manufacturing material data was obtained.

The predicted burst speed is about $0.834\omega_{Burst}^{Exp.}$ – $0.877\omega_{Burst}^{Exp.}$ according to the linear elastic analysis, based on average material data, 50% casted + 50% forged Inco 718. If fully forged material are assumed, the maximum burst speed would approximately increase with 7.65%. The plastic analysis tended to predict a higher burst RPM, up to $0.991\omega_{Burst}^{Exp.}$.

The original mesh was develops by GKN Aerospace using *ANSYS Mechanical APDL* when performing the before hand over-speed burst study, see Fig. A.1. It consisted of 474493 nodes and 319797 ten-noded tetrahedral element (TET10) and was developed using *ANSYS Mechanical APDL*.

Elastic burst margin criteria	$\omega_{\mathbf{Burst}}^{\mathbf{Exp.}}$
(AWMHS) NASA	0.8768
Hallinan	0.8341
Radial NASA	0.8597

Table A.0: Burst margin calculation performed during the prestudy.

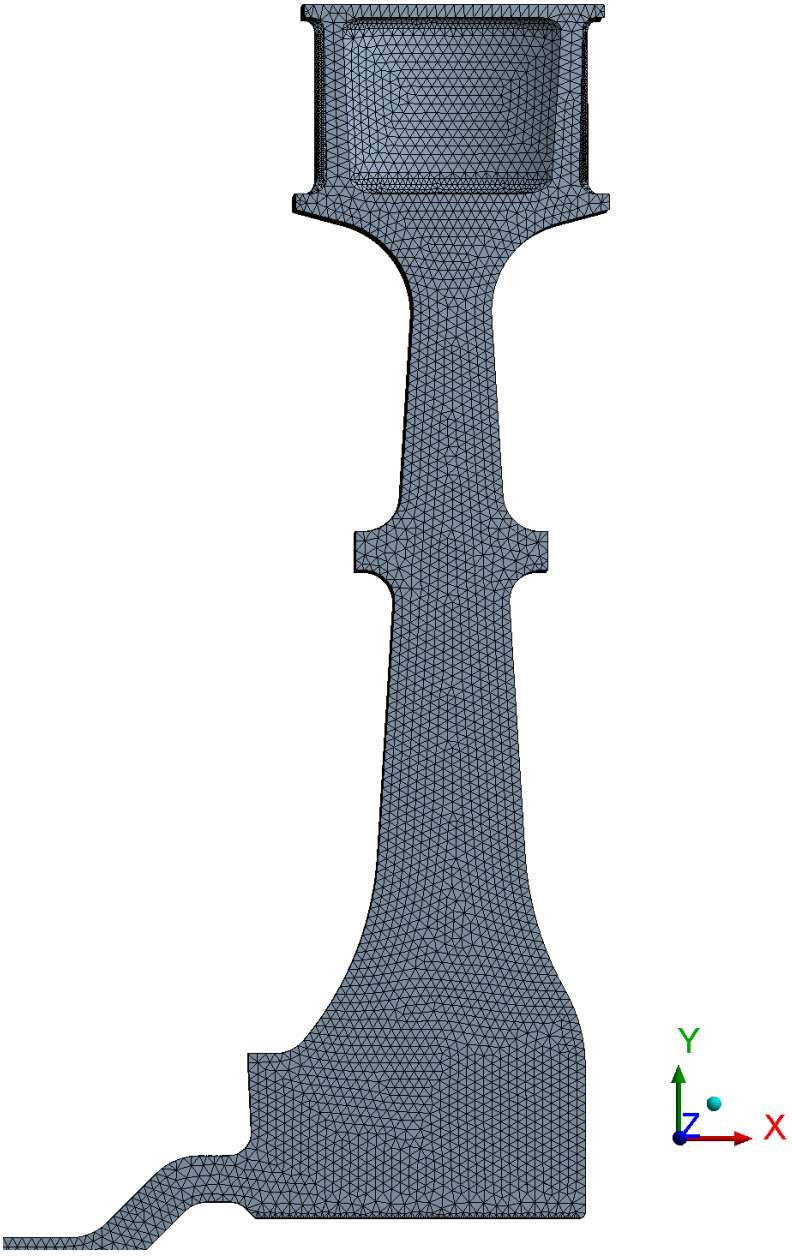

Figure A.1: Mesh used to perform the prestudy simulations.

B Rotor burst experiment summery

The following report is a limited summery of the experimental burst test, *Test Synthesis: Rotor Burst Test in Prometheus* (VOLS:10262172).

B.1 Introduction

Rotor burst test was conducted for the Prometheus project to validate the necessary safety requirements when developing new rotor designs. The test was conducted by successively increasing the rotational velocity until the Prometheus demonstrator rotor bursted, see Fig. B.1.

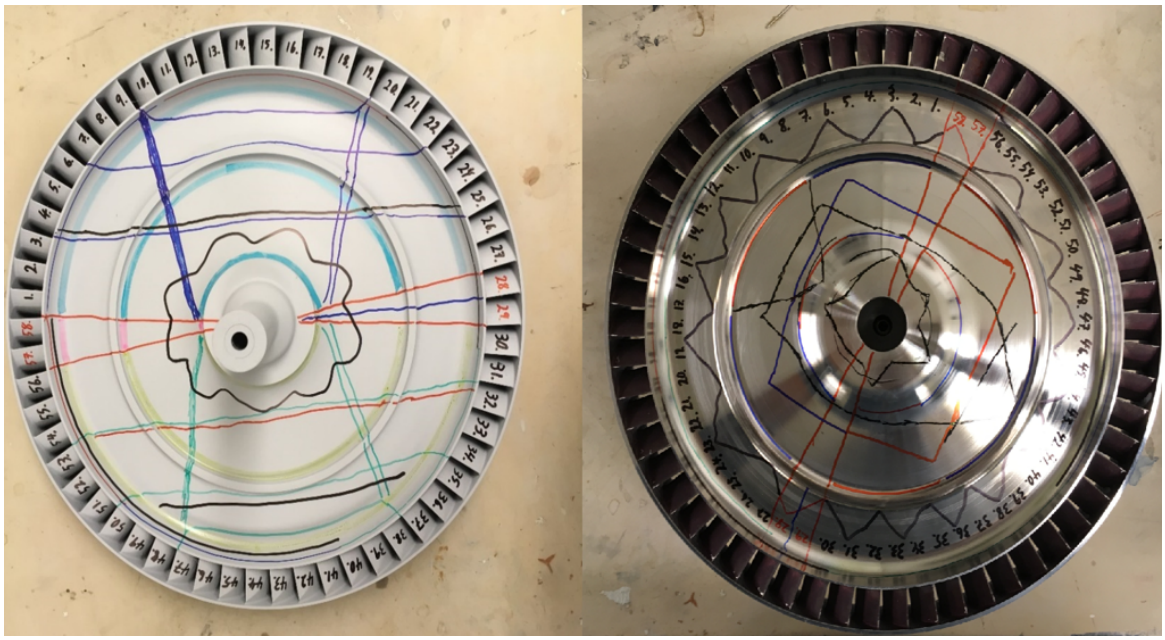

Figure B.1: Upstream and downstream side of the Prometheus demonstrator turbine, respectively.

B.2 Test setup

The experiment was performed in GKN Aerospace Sweden test cell for spin tests in shop X which is powered by a drive turbine. The test turbine is placed in vacuum chamber which is not fully vacuumized. Rotational speed sensor was used to gather data during the test. The rotor was balanced prior to the painting.

B.3 Rotor experimental burst test results

The failure occurs at about 896s as seen in Fig. B.3 and after conclusions were drawn, the location of the initial fracture is assumed to be between the lower disc and the balancing flange, see Fig. B.2.

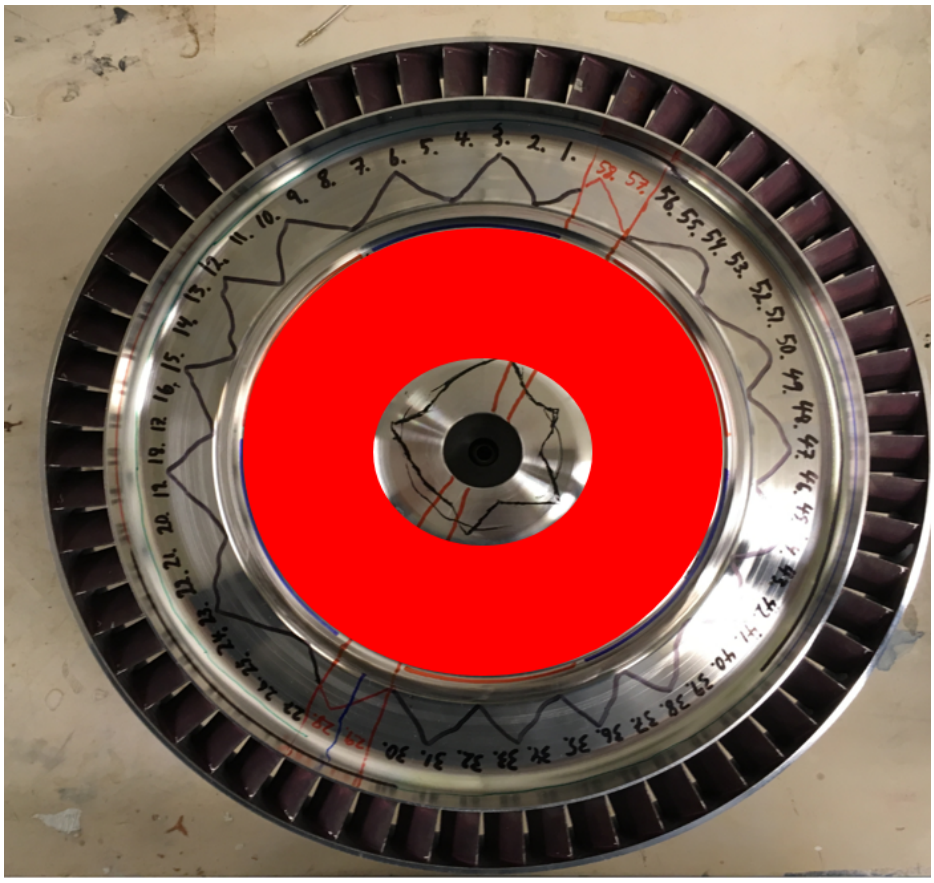

Figure B.2: Assumed location where initial burst fracture occurred.

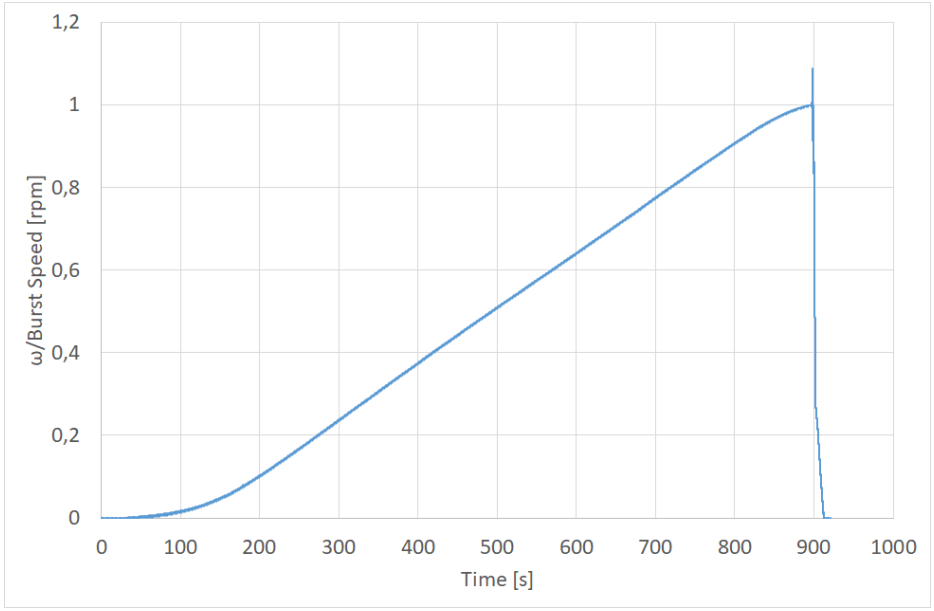

Figure B.3: Recorded rational velocity during the Prometheus demonstrator rotor burst test.